



# Dating Granites Using CODEX, with Application to In Situ Dating on the Moon

Jonathan Levine<sup>1</sup>, F. Scott Anderson<sup>2</sup>, Sarah Braden<sup>3</sup>, Rico G. Fausch<sup>4</sup>, Sean Foster<sup>1,5</sup>, Gavin Fowler<sup>1</sup>, Katherine H. Joy<sup>6</sup>, Steven Osterman<sup>2</sup>, John Pernet-Fisher<sup>6</sup>, Stephen Seddio<sup>7</sup>, Tom Whitaker<sup>2</sup>, Peter Wurz<sup>4</sup>, Marcella Yant<sup>8</sup>, and Teng Ee Yap<sup>1,9</sup>

<sup>1</sup>Department of Physics and Astronomy, Colgate University, 13 Oak Drive, Hamilton, NY 13346, USA; [jlevine@colgate.edu](mailto:jlevine@colgate.edu)

<sup>2</sup>Southwest Research Institute, Suite 300, 1050 Walnut Street, Boulder, CO 80302, USA

<sup>3</sup>Boulder, CO, USA

<sup>4</sup>Space Research & Planetary Sciences, The University of Bern, Sidlerstrasse 5, CH-3012 Bern, Switzerland

<sup>5</sup>Current address: Department of Physics, Boston University, 590 Commonwealth Avenue, Boston, MA 02215, USA

<sup>6</sup>Department of Earth and Environmental Sciences, The University of Manchester, Oxford Road, Manchester, M13 9PL, UK

<sup>7</sup>Thermo Fisher Scientific, 5225 Verona Road, Fitchburg, WI 53711, USA

<sup>8</sup>Lockheed Martin Space, Littleton, CO, USA

<sup>9</sup>Current address: Division of Geological and Planetary Sciences, California Institute of Technology, Pasadena, CA 91125, USA

Received 2023 January 5; revised 2023 March 26; accepted 2023 April 13; published 2023 May 22

## Abstract

We have measured  $^{87}\text{Rb}$ – $^{87}\text{Sr}$  isochron ages for two granites, using the breadboard version of our Chemistry, Organics, and Dating EXperiment (CODEX), a laser-ablation resonance-ionization mass spectrometer designed for in situ geochronology on the Moon or Mars. These measurements extend the demonstrated analytical capabilities of CODEX, and indicate the value of incorporating a flight-ready version of CODEX, now under construction, into a future mission payload. We used CODEX to obtain accurate ages for the 1700 Ma Boulder Creek Granite, with  $1\sigma$  statistical precision of 110 Myr, and for the 1100 Ma Pikes Peak Granite, with  $1\sigma$  statistical precision of 160 Myr. To provide an end-to-end illustration of how CODEX analysis of granites can address critical lunar science questions regarding rock age and composition in situ, we describe an example mission to the lunar Gruithuisen Domes. Gruithuisen Domes appear to be volcanic edifices of granitic composition. Orbital remote sensing suggests that granitic rocks represent only a small fraction of the lunar surface, and the mere fact of their existence on the Moon is a puzzle. CODEX determination of the timing and process of their formation, both presently ill-understood, would provide important constraints on the thermal and geochemical evolution of the lunar interior.

*Unified Astronomy Thesaurus concepts:* [The Moon \(1692\)](#); [Lunar geochronology \(954\)](#); [Space vehicle instruments \(1548\)](#); [Lunar evolution \(952\)](#)

## 1. Introduction

### Highlights:

1. Dating rare silica-rich granitic formations on the Moon is key to understanding lunar magmatic evolution.
2. For lunar analog granites, we obtain ages and  $1\sigma$  confidence intervals of  $1780 \pm 110$  Ma (Boulder Creek Granite) and  $1030 \pm 160$  Ma (Pikes Peak Granite) using our breadboard version of CODEX, an in situ dating instrument.
3. We outline a mission to date the Gruithuisen Domes on the Moon using CODEX, and the science such a mission would deliver.

For two decades, we have been developing a spaceflight laser-ablation resonance-ionization mass spectrometer called CODEX, the Chemistry, Organics, and Dating Experiment (e.g., Anderson et al. 2003). Our breadboard version is a fully operational laboratory-scale instrument, which we have successfully used to date the Martian meteorite Zagami (Anderson et al. 2015a, 2020b) and the Duluth Gabbro (Anderson et al. 2015b). Both of these examples have mineral assemblages and chemical compositions typical of basalts, which are widespread in the crusts of the terrestrial planets

(gabbros differ from basalts primarily in grain size). Granitic rocks, by contrast, have long been more tempting targets for CODEX dating than basalts or gabbros, because granitic magmas tend to concentrate large-ion lithophile elements like Rb, whose radioactive decay is the chronometer exploited by CODEX. In the present work, we have successfully dated specimens of the Boulder Creek and Pikes Peak Granites (Colorado, USA), and we illustrate here how femtosecond laser ablation and empirical noise removal have permitted us to extract meaningful geochronological data from these samples.

Though Earth is unique among solar system bodies for its quantity of granitic rocks and their extent of magmatic evolution, granitic rocks in low abundances are also inferred on the Moon, on the basis of (i) a small mass of granitic fragments included among the Apollo samples (e.g., Ryder et al. 1975; Seddio et al. 2014), (ii) granitic clasts in lunar meteorites (e.g., Bechtold et al. 2021), and (iii) spectroscopic anomalies interpreted to be outcrops of especially silica-rich and iron-poor rocks (e.g., Glotch et al. 2010). Here, and throughout this paper, we use the term “granitic” loosely to describe igneous rocks of  $\gtrsim 65\%$   $\text{SiO}_2$  with associated alkali or K-rich feldspar, irrespective of texture or inferred cooling rates. Granites on Earth are most often the result of crustal recycling, so the fact that granitic rocks are present on the Moon, without extensive crustal recycling, and in the near absence of water, is something of a surprise (Ryder 1976). The geochemistry and geochronology of lunar granitic outcrops are important clues to understanding the evolution of the interior of the Moon.



Original content from this work may be used under the terms of the [Creative Commons Attribution 4.0 licence](#). Any further distribution of this work must maintain attribution to the author(s) and the title of the work, journal citation and DOI.

Both geochemical and geochronological data can be acquired by CODEX, which operates in two distinct modes. As a laser-ablation mass spectrometer, CODEX analyzes elemental abundances of rock specimens on the mineral scale. As a laser-ablation resonance-ionization mass spectrometer, CODEX sensitively analyzes isotopic abundances of Rb and Sr for isochron dating. In this way, CODEX is both a geochemical instrument and a geochronological instrument. Our first goal in this paper is to describe our latest advances using our laboratory breadboard CODEX for dating. Our second goal is to illustrate the scientific utility of CODEX, as both a geochemical and geochronological tool, with a mission concept to study the geochemically evolved magmas at the lunar Gruithuisen Domes (Braden & Robinson 2011). Age estimates for these domes (Wagner et al. 2002; Braden 2013; Ivanov et al. 2016) are difficult to reconcile with chemical models of how granitic magma may have been erupted there (e.g., Ivanov et al. 2016), so a direct measurement of their age would be particularly valuable.

Building on the present work and other demonstration experiments with the breadboard, progress toward a flight version of CODEX has been underway since 2014, including brassboard laser systems and incorporation of a miniature time-of-flight analyzer. The authors of this work constitute a collaboration among the developers of the CODEX breadboard, planetary geochronologists and geochemists, and the developers of spaceflight mass spectrometers for geochemical analysis. We leverage all of our collective experience to understand the composition of evolved magmas erupted at the Gruithuisen Domes, and to place their origin into the timeline of lunar history.

## 2. Scientific Context for Solar System In Situ Dating

One significant legacy of the Apollo missions is that the returned lunar samples have permitted the development of an absolute chronology of much of lunar history (e.g., Neukum et al. 1975). However, there remain many important questions about the history of the Moon that the Apollo samples cannot address (e.g., Tartèse et al. 2019), because sampling was sparse, most collected rocks are unprovenanced, and most landing sites were affected by the Imbrium impact (e.g., Spudis et al. 2011). We (Anderson et al. 2020a) and other authors (Zellner 2017; Cohen et al. 2021) have recently outlined the most important outstanding questions of lunar chronology, so we present only a brief summary here, and we call out for particular mention the questions that concern granitic rocks. In this section, we discuss the unknowns of lunar dating in the context of the major stratigraphic units recognized on the Moon (Shoemaker & Hackman 1962; Wilhelms et al. 1987), and we calculate the dating precision necessary to answer those key questions.

### 2.1. Pre-Nectarian and Nectarian Periods

The Pre-Nectarian and Nectarian periods (approximately 4500–3920 Ma) include the crystallization of the lunar magma ocean and the formation of most giant impact basins. The ages of most basin-forming impacts are either unknown (Norman 2009) or contested. For example, the Nectaris impact itself has been suggested to have occurred as early as 4250 Ma (Schaeffer & Husain 1974), but alternatively as late as 3900 Ma (James 1982). The difference is not merely academic, because

the Nectarian period ends with the Imbrium impact, for which a 3920 Ma age is presently favored (Liu et al. 2012; Nemchin et al. 2021); therefore, the whole of the Nectarian period, with 11 giant impact basins belonging to it (Fassett et al. 2011), either took  $\sim 300$  Myr or was geologically instantaneous. If the latter, a dynamical mechanism is required for suddenly delivering a large number of giant meteoroids to the Moon long after most planetary accretion had concluded, but if Nectaris is older, no such “lunar cataclysm” (Tera et al. 1974) may have occurred. To distinguish with 95% confidence among an “old” Nectaris that formed 4250 Ma, a Nectaris that is 300 Myr younger, or an intermediate age, we have argued (Anderson et al. 2020a) that its melt sheet or ejecta would need to be dated with  $\sim 75$  Myr precision (all uncertainties herein are  $1\sigma$ ). This precision requirement is stronger than that proposed by Cohen et al. (2021). Only if the precision exceeds one quarter of the time interval in question is it possible to say with 95% confidence if an intermediate age, rather than either end-member age, is correct.

It is to the Pre-Nectarian and Nectarian periods that most of the known lunar granitic samples belong. To give just a few examples, Zhang et al. (2012) and Thiessen et al. (2018) measured 4150–4300 Ma  $^{207}\text{Pb}/^{206}\text{Pb}$  ages for multiple zircon crystals from granitic clasts in Apollo 12 breccia 12013. Meyer et al. (1996) recognized a period of lunar granophyre production from 4230–3880 Ma. Grange et al. (2013) dated zircon crystals in a quartz monzodiorite clast of Apollo 15 breccia 15405 to  $4330 \pm 6$  Ma. A survey by Seddio et al. (2014) of lunar granophyres found that 11 out of 14 were older than 3900 Ma. Likewise, Zeng et al. (2021) identified a granitic fragment in lunar meteorite Northwest Africa 10447, and dated it to 4320 Ma. This strong preponderance of Nectarian and Pre-Nectarian ages among lunar granitic materials begs the question of how the Moon can have evolved silicic magmas so early, and where within the Moon granitic magmas were sourced.

### 2.2. Imbrian and Eratosthenian Periods

The Imbrian and Eratosthenian periods (approximately 3920–800 Ma) include the final giant basin-forming impacts (Imbrium, Schrödinger, and Orientale), and most of the great eruptions of basaltic lava that constitute the lunar maria. Mare volcanism apparently originated with the remelting of cumulates that crystallized from the lunar magma ocean, but the heat source to melt those rocks, hundreds of millions of years after the magma ocean solidified, is still not understood (Grove & Krawczynski 2009; Laneuville et al. 2013). The ages of most maria are estimated on the basis of crater size-frequency distributions (e.g., Neukum 1977; Hartmann et al. 1981; Neukum et al. 2001), but improved imaging from Lunar Reconnaissance Orbiter has led to challenges to older estimates of crater densities (Robbins 2014). The model of Robbins (2014), for example, infers ages for certain terrains of up to 1100 Myr younger than had been suggested by the work of Neukum et al. (2001). The chronology of Robbins (2014) doubles the duration for the era of peak mare volcanism, which requires a longer-lived heat source in the lunar interior. Moreover, because the crater-based chronology of the Moon underpins the estimates of surface ages on other planetary bodies, the Robbins (2014) chronology implies a considerably longer habitable era on Mars.

Recently, important tests of these chronologies have been carried out using lunar samples collected by Chang'e 5. Measured ages of  $2030 \pm 4$  Ma (Li et al. 2021) and  $1963 \pm 57$  Ma (Che et al. 2021) more closely accord (Yue et al. 2022) with the chronology of Neukum et al. (2001), given the crater density at the Chang'e 5 landing site. One particular surprise associated with the Chang'e 5 samples is that they are relatively poor in the so-called KREEP elements (potassium, rare-earth elements, and phosphorus; Tian et al. 2021), which include heat-producing K, Th, and U, and so they invite continuing investigation of the heat sources for magma production as late as  $\sim 2000$  Ma (Che et al. 2021; Du et al. 2022). The observation that the Chang'e 5 samples are geochemically unrepresentative of the Procellarum KREEP terrane (Wieczorek & Phillips 2000) from which they were sourced invites the question of whether they are also chronologically atypical. Addressing this question will require additional age measurements from Eratosthenian terranes. Given the magnitude of the discrepancy between the proposed chronologies, the exquisite precision afforded by a sample-return mission, as demonstrated by Li et al. (2021), is not required; rather, it is sufficient to achieve dating precision of a few hundred million years, so in situ dating experiments potentially have much to contribute (Anderson et al. 2020a).

An interesting geochronological mystery of the Imbrian period concerns the Gruithuisen Domes. Situated on the margin of the Imbrium basin, these domes have steeper slopes ( $>10^\circ$ ) and larger volume ( $780 \text{ km}^3$ ) than the volcanic domes that characterize the lunar maria (Wöhler et al. 2006; Ivanov et al. 2016), suggesting they were constructed by relatively viscous, Si-rich lava. Geochemical support for this inference comes from the detection of elevated Si concentration by the Lunar Reconnaissance Orbiter Diviner Radiometer (Glotch et al. 2010; Greenhagen et al. 2010a, 2010b), relatively low abundances of Fe- and Mg-rich silicates by the mineralogy mappers on board Chandrayaan-1 (Kusuma et al. 2012) and SELENE/Kaguya (Lemelin et al. 2019), and elevated Th concentrations by the Lunar Prospector Gamma Ray Spectrometer (Lawrence et al. 2003). Enrichment in Th is a hallmark of the Procellarum KREEP Terrane (Jolliff et al. 2000); however, the Th concentrations inferred by Hagerty et al. (2006) at Gruithuisen Domes are  $\sim 8$  times higher than the enrichment for the Procellarum KREEP Terrane as a whole (Jolliff et al. 2000). The very high concentrations of Th—and presumably K and U, which are likewise large-ion lithophile elements and radioactive—suggest that the geochemical and thermal conditions for unusual lunar volcanism were present at the Domes (Jolliff et al. 2000).

The mechanism that produced such a large quantity of granitic magma at Gruithuisen Domes is not known. If it were the result of fractional crystallization of Imbrium melt, the age of the Domes ought to be indistinguishable from the age of Imbrium itself, at 3920 Ma. However, if the granitic magma were a crustal melt generated by underplating by basaltic magma (e.g., Hagerty et al. 2006), Gruithuisen Domes should have an age comparable to the ages of the surrounding basaltic plains, which are estimated to be younger than 3600 Ma (Ivanov et al. 2016). Precision of  $\leq 80$  Myr would be required to distinguish between these hypotheses.

On the basis of crater counts, Wagner et al. (2002), Ivanov et al. (2016), and Braden et al. (2014) have estimated the ages of the Domes. All of these studies conclude that Gruithuisen

Domes are younger than the Imbrium impact, and only the age estimate of Braden et al. (2014) coincides with the age of the surrounding basaltic plains. However, the age estimate of Braden et al. (2014) is resolvably different from the other two studies. In view of the continuing mystery of when Gruithuisen Domes formed, we revisit their origin in Section 5.

### 2.3. Copernican Period

The Copernican period (approximately 800 Ma to the present) includes the formation of the bright-rayed craters Copernicus, Aristarchus, and Tycho, and, apparently, small volcanic eruptions that have created the so-called irregular mare patches (Braden et al. 2014). There is evidence from the Moon that the rate of meteoroid bombardment has increased severalfold during the Copernican period (e.g., McEwen et al. 1997; Culler et al. 2000; Levine et al. 2005; Mazrouei et al. 2019), which is interesting since this time interval overlaps all of the Phanerozoic on Earth, with its repeated swings in biodiversity, some of which are attributable to meteoroid impacts (Alvarez et al. 1980).

While there are no reports in the literature of any lunar granitic rocks that originate in the Copernican period, the Aristarchus crater and its ejecta tap into a reservoir of material enriched in potassium, rare-earth elements, and phosphorus with elevated Th concentrations (Lawrence et al. 2007), so even some of the most recent lunar impacts continue to rework geochemically evolved material.

The absolute ages of some events in Copernican time are necessarily uncertain, because the age of the Copernicus crater is itself uncertain. It was radioisotopically dated to  $800 \pm 40$  Ma by Eberhardt et al. (1973), on the assumption that the analyzed material (glass enriched in KREEP collected  $\sim 400$  km away, at the Apollo 12 landing site) was ejecta specifically from Copernicus. A more recent estimate, based on the density of  $>1$  km craters superimposed on Copernican ejecta, constrains the age of Copernicus only to the interval 519–1230 Ma (Hiesinger et al. 2012). The width of this interval is an indication of the need for additional radioisotopic ages for lunar samples from throughout lunar history.

We have been developing the CODEX instrument in order to fill such gaps in our understanding of lunar history. The flight version of CODEX, described in Section 5.3, is designed to be compact and portable, and requires no sample preparation except for grinding a flat surface. The breadboard instrument in one demonstration successfully dated the Martian meteorite Zagami with 20 Myr precision (Anderson et al. 2020b). The composition of Zagami is basaltic; here we demonstrate the first uses of the breadboard CODEX to date granitic rocks as well.

### 3. Method: Dating Using CODEX

CODEX normally uses the  $^{87}\text{Rb}$ – $^{87}\text{Sr}$  isochron dating method, which has been applied to a wide range of igneous rocks from Earth, as well as lunar and Martian meteorites. The principles of  $^{87}\text{Rb}$ – $^{87}\text{Sr}$  dating are described in detail by, for example, Faure (1986). In brief, the accumulation of radiogenic  $^{87}\text{Sr}$  from  $^{87}\text{Rb}$  decay is described by:

$$\left(\frac{^{87}\text{Sr}}{^{86}\text{Sr}}\right) = \left(\frac{^{87}\text{Sr}}{^{86}\text{Sr}}\right)_{\text{initial}} + \left(\frac{^{87}\text{Rb}}{^{86}\text{Sr}}\right)(e^{\lambda t} - 1) \quad (1)$$

in which  $\lambda = (1.3972 \pm 0.0045) \times 10^{-11} \text{ yr}^{-1}$  is the decay constant for  $^{87}\text{Rb}$  (Villa et al. 2015) and  $t$  is the time elapsed

since the formation of the minerals in the sample. Because minerals in a rock partition Rb and Sr differently, each represents a different solution to Equation (1). For unaltered rocks, Equation (1) predicts linear variation between measured  $^{87}\text{Rb}/^{86}\text{Sr}$  ratios and  $^{87}\text{Sr}/^{86}\text{Sr}$  ratios among the minerals in a rock crystallized at a single time; the slope of the line relating these measurements is the factor  $e^{\lambda t} - 1$ , and so determines the age  $t$ . A key advantage of isochron analysis over single measurements of the radioactive isotope and its daughter product is that differential alteration of rock can be diagnosed if the measurements do not obey the predicted linear relationship. In addition to our work in the Rb/Sr system, we have also demonstrated the use of our breadboard CODEX for Pb-Pb isochron dating with a precision of 50 Myr (Anderson et al. 2020a).

For dating, CODEX measures the abundances of Rb and Sr isotopes in dozens to hundreds of small spots on a rock sample. Applicability to spaceflight has guided all stages in the development of CODEX. For example, analysis spots on each specimen are probed by laser ablation, rather than by ion sputtering, because laser ablation requires less power and provides higher count rates, necessary to meet precision requirements in less mission time. Atoms of Rb and Sr in each ablation plume are selectively ionized by laser light tuned to electronic resonances characteristic of each element. Resonance ionization is particularly well suited to spaceflight applications because it permits high sensitivity and elemental selectivity. Moreover, it avoids the need for complicated sample-handling procedures, other than the grinding of a flat surface onto a rock specimen to ensure that all spot analyses are acquired in the focal plane of the ablation laser. The ions generated by resonance ionization are injected into a time-of-flight mass analyzer. The mass analyzer in the CODEX breadboard is a multibounce unit built as a brassboard model for MASPEX (Sephton et al. 2018), part of the instrument suite for Europa Clipper, which is scheduled for launch in 2024 October. We have also experimented with a much smaller reflectron time-of-flight analyzer developed at the University of Bern, with spaceflight heritage in the ROSINA instrument (Balsiger et al. 2007), and whose design we are adopting for the flight version of CODEX.

The CODEX breadboard has allowed us to determine requirements for the flight lasers and mass spectrometer, such as optimal pulse-lengths, wavelengths, and intensities. In some cases, we have chosen hardware for the breadboard that is larger than can be used for flight, but which enabled exploration of wider ranges of operational parameters. For example, the present experiment used an ablation laser (Kapteyn–Murnane Laboratories Wyvern) that emits 150 fs pulses with far greater intensity ( $\sim 40 \text{ TW cm}^{-2}$ ) than is presently available in flight-sized systems. As will be seen, femtosecond ablation fractionates elements much less than does nanosecond ablation; nevertheless, our experience with nanosecond ablation suggests that it is sufficient to address many science questions. We have found (Anderson et al. 2020b) that femtosecond ablation improved our dating precision on the Zagami meteorite by about a factor of 2, but that other manipulations of the sample, such as keeping it  $\sim 1 \text{ mm}$  back from the entrance aperture to the mass analyzer, were even more significant, having improved our dating precision by an additional factor of 4.

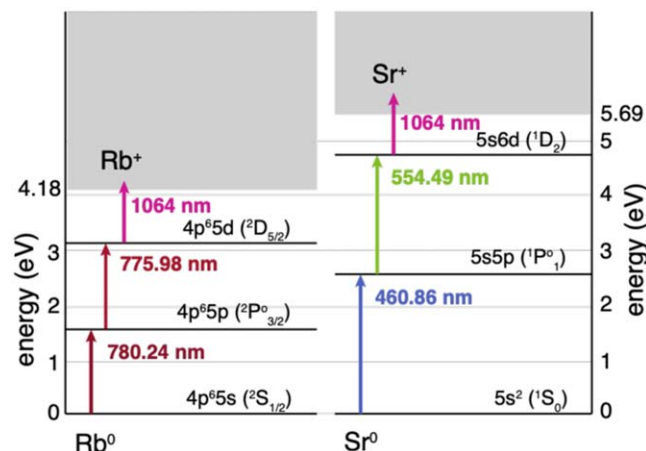


**Figure 1.** Electronic resonances in neutral Rb and Sr excited by tuned lasers in this experiment. For both Rb and Sr, successive absorption of one photon from each of the three lasers suffices to promote the atoms above the ionization energy.

In the present experiment, we used the breadboard CODEX to analyze two granite samples that were prepared only by hand-polishing to  $< 50 \mu\text{m}$  of surface topography. Femtosecond laser pulses vaporized  $\sim 80 \mu\text{m}$  spots on the samples, generating transient plumes of ions, neutral atoms, and perhaps polyatomic clusters. Some of the ions, atoms, and clusters entered the source region of the mass spectrometer through a 1 mm aperture in a metal plate. In order to reduce interferences with the isotopes of Rb and Sr that we sought to detect, we electrostatically pushed positively charged ions back toward the plate for  $\sim 2 \mu\text{s}$  to exclude them from the time-of-flight mass analyzer. Then, we reversed the direction of the electric field and used tuned lasers to selectively excite and ionize neutral Sr atoms, followed  $\sim 2 \mu\text{s}$  later by neutral Rb atoms from the same ablation plume. Details of the laser excitation scheme and the electronic resonances they exploit are shown in Figure 1. By delaying the photoionization of Rb relative to Sr, we likewise delayed the entry of Rb into the time-of-flight mass analyzer and its subsequent arrival at the detector. In this way, the detector signal separately recorded the arrival of each isotope of Sr and Rb, and suppressed the isobaric interference between  $^{87}\text{Rb}$  and  $^{87}\text{Sr}$ .

The lasers used to excite Sr atoms from the ablation plumes were an OPOTek Opolette 355 LD tuned to 460.86 nm ( $\sim 100 \mu\text{J}$ ,  $\sim 10 \text{ ns}$  pulses), a Coherent Scanmate Pro using fluorescein 548 dye tuned to 554.49 nm ( $\sim 1 \text{ mJ}$ ,  $\sim 10 \text{ ns}$  pulses), and a Quantel YG-980 Nd:YAG that produces 1064 nm light in  $\sim 100 \text{ mJ}$ ,  $\sim 10 \text{ ns}$  pulses for photoionization. The lasers exciting Rb were similar, except in wavelength: another OPOTek Opolette 355 LD drove the first resonance with 780.24 nm light, a Continuum ND6000 with LDS-765 dye tuned to 775.98 nm drove the second resonance, and a Continuum Powerlight 8020 Nd:YAG produced 1064 nm light for photoionization.

Ions from the granite samples were sent through seven round-trips of the multibounce time-of-flight mass analyzer. We found that this number of bounces yielded the greatest signal-to-noise ratio (S/N), by focusing arrival times at the detector for ions of each species.

In each experimental run, we analyzed up to 626 spots on  $< 100 \text{ mm}^2$  regions of each specimen, thus sampling the suite



**Figure 2.** Photomicrograph of standard GSD-2G (left) and Boulder Creek Granite (right), showing ablation pits in both. The ablation pits, which define a rectangular grid of points separated by 0.2 mm, sample multiple mineral phases in the granite. The field of view is about 13 mm across. After these analyses were acquired, the sample mount was re-polished to flatness, and a new grid of points analyzed.

of different minerals in each rock (Figure 2). At each spot, we first conditioned the sample surface with 1000–10,000 ablation shots. Conditioning shots were delivered at 1 kHz, so the conditioning took 1–10 s. Next, we acquired time-of-flight spectra at 20 Hz from 2000 ablation shots in 10 interleaved sets, each of which included 100 shots with all Rb and Sr resonance lasers turned on, and 100 shots with the some or all of the resonance lasers turned off. The latter spectra permit us to measure the background of ions produced nonresonantly by each laser.

We bracketed every four spot analyses of the specimens with an analysis of a piece of GSD-2G glass (Wilson 2018) mounted alongside each. This reference material was developed by the United States Geological Survey as a replacement for the better-known GSD-1G (Jochum et al. 2011), with nearly identical abundances of elements and isotope ratios. However, the concentrations of trace elements in GSD-2G are not as well determined as in GSD-1G, and the  $\sim 10\%$  uncertainties in the concentrations of Sr and Rb are leading contributors to the uncertainties in the rock ages we present here. Additional measurements by the scientific community of GSD-2G will undoubtedly reduce this uncertainty in the future. For this reason, we present our age determinations with statistical errors (i.e., random measurement uncertainties derived from the CODEX dating approach) separated from systematic errors (uncertainties in the composition of GSD-2G and in the decay constant of  $^{87}\text{Rb}$ ).

The resonance lasers used in this experiment operate at a repetition rate of 20 Hz, so spot analyses with several thousand laser shots took a few minutes to acquire. Generation of an isochron with several hundred spot analyses took tens of hours. The flight models of these lasers run at 1–10 kHz, and therefore will require much less measurement time (Section 5).

The data presented in this paper were acquired in 2019, before we learned that leaving a gap of  $\sim 1$  mm between the sample and the entry electrode of the mass spectrometer helps our S/N by preferentially diminishing the penetration of plasma into the mass spectrometer (Anderson et al. 2020b). Therefore, the many of time-of-flight spectra we obtained on these granites are noisier, by several times, than those we obtained since. Moreover, the signals we detected in this work, especially for Sr, which usually is less efficiently ionized than Rb, are small compared with what we have found in other experiments. The smallness of our signals could have been caused by the gradual sputter coating of a prism, subsequently replaced, inside the instrument, which delivers the ablation laser beam onto the sample. It takes about 20 samples to

noticeably degrade the prism, which, for flight, will limit the total sample throughput, or require a larger, movable prism; for most missions, however, 20 samples is sufficient to address the science. The relatively small signals and the relatively high noise level made these data sets look unattractive when we obtained them in 2019, but here we show that we obtained meaningful age information from both granites in spite of their noisy backgrounds.

The noise we observed included both electronic noise and the counting of background ions created by processes other than resonance ionization of Rb and Sr. For example, for granites more than for other rocks, there is often a diffuse (in time) background that we attribute to ions of diverse mass having entered the mass spectrometer in the plasma plumes from ablation. Such ions arrive at the detector at a wide range of times because electrical interactions in the plasma interfere with the electric fields we impose to accelerate and focus ions onto the detector. We subtracted this background by fitting our spectra, with their Rb and Sr peaks masked out, either to a line or to a “swell” shape, consisting of the product of rising and falling hyperbolic tangent functions. For the swell shape, we fit a five-parameter empirical function:

$$b_{\text{diffuse}}(t) = c_1 [\tanh(c_2(t - c_3)) + 1] \times [\tanh(c_4(c_5 - t)) + 1], \quad (2)$$

where  $b_{\text{diffuse}}$  is the diffuse background,  $t$  is the time of flight, and  $c_{1-5}$  are five adjustable parameters. This function is a relatively simple implementation of an asymmetric peak that falls to zero on both sides: the first bracketed factor smoothly rises from a value of 0 to 2, increasing most rapidly near  $t = c_3$ , and having a slope there of  $c_2$ . The second bracketed factor smoothly falls from 2 to 0, decreasing most rapidly near  $t = c_5$  and having a slope there of  $-c_4$ . The entire function is scaled in magnitude by the factor  $c_1$ . We used a nonlinear least-squares optimization algorithm in Matlab to find the parameters  $c_{1-5}$  that best fit the diffuse background for each spot analysis, and then subtracted away this best fit to the diffuse background. About 95% of spectra were well fit by these empirical functions (e.g., Figure 3), and because the remaining 5% of spots continued to show large uncorrected interferences from background noise, we removed them from the isochron analysis.

In addition to diffuse background noise, in some spectra we saw evidence of Rb atoms ablated directly into excited electronic states, which are ionized by the 461 nm laser intended to excite neutral ground-state Sr. Atoms of  $^{87}\text{Rb}$  ionized by these lasers, as opposed to being ionized by the lasers tuned to Rb resonances, which fire  $2 \mu\text{s}$  later, arrived at the detector at the same time as  $^{87}\text{Sr}$ , and are therefore a potential interference. Though we directly measured this background and subtracted it, its shot-to-shot fluctuations made it difficult to quantify  $^{87}\text{Sr}$  in spots with very high Rb/Sr ratios. In addition, in spite of the  $2 \mu\text{s}$  given over to repulsion of ions created directly by the ablation process, some such ions succeeded in reaching the detector. Since they were accelerated from closer to the sample than are the resonantly excited photoions, they were less well focused in their arrival times at the detector; also, since they were electrically charged before the resonance lasers fired, they arrived at the detector earlier than the photoions.

Though Rb ions due to ablation were easily distinguished from resonantly photoionized Rb ions, we often found that the

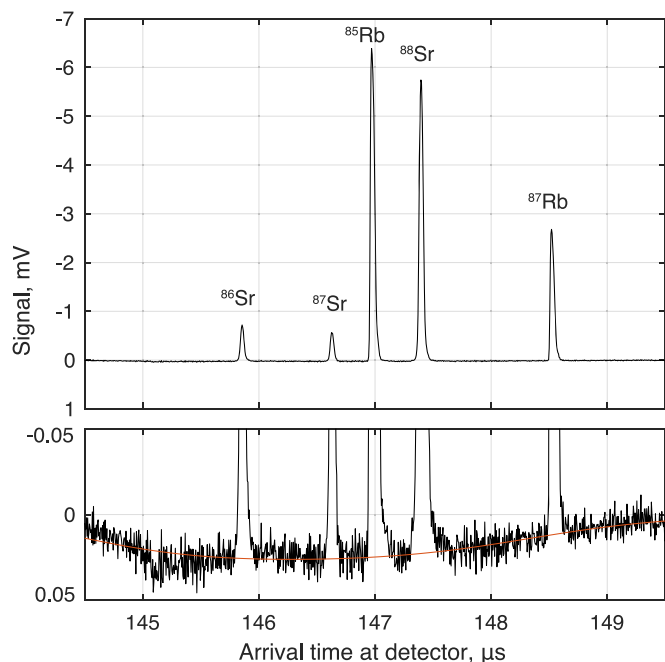


**Figure 3.** Time-of-flight spectrum for Boulder Creek Granite spot analysis 20190723bcg\_gsd-2g\_ras\_150, after subtracting measured backgrounds. Measured backgrounds are meant to quantify ions due to ablation and to individual resonance lasers. In principle, the only signal remaining should come from ions produced by the resonance lasers acting in tandem, i.e., Rb and Sr. Top: spectrum at full scale. Bottom: baseline region of the same spectrum, magnified to show the diffuse background remaining after subtraction of the measured backgrounds. We fit the remaining background with an empirical function representing a swell by the product of rising and falling hyperbolic tangent functions (red). There also appears to be incomplete subtraction of a background peak at 145.1  $\mu\text{s}$ , but fortunately this does not interfere with any of the resonance ionization peaks.

noise of  $^{87}\text{Rb}$  ions from ablation interfered with the detection of  $^{86}\text{Sr}$  photoions (Figure 4). Because this problem was especially pronounced during our analyses of Pikes Peak Granite, for that specimen we followed Anderson et al. (2015b) in using  $^{88}\text{Sr}$  instead of  $^{86}\text{Sr}$  to quantify the nonradiogenic Sr present in each spot.

Of the hundreds of spot analyses that we obtained on each sample, we retained for isochron analysis only those with  $S/N_s \geq 2$  for each of the five isotopes  $^{86,87,88}\text{Sr}$  and  $^{85,87}\text{Rb}$ . We compared our measurements of  $^{86}\text{Sr}$  and  $^{88}\text{Sr}$  with their natural ratio of 0.1194 (Meija et al. 2016) to assess the extent of instrumental isotopic fractionation, which we assume to have been mass-dependent, and we corrected measurements of  $^{87}\text{Sr}$  accordingly.

We used our measurements of GSD-2G to monitor the instrumental sensitivity to each isotope, as well as how each varied with time. For example, in the time-of-flight spectrum shown in Figure 3, Rb isotopes were over-detected relative to Sr by a factor of about 3.5, and  $^{87}\text{Sr}$  is under-detected relative to the even-mass Sr isotopes by about 19%. Elemental fractionation can arise from the different transition strengths of the Rb and Sr electronic resonances, the different intensities of the lasers tuned to those resonances, the fact that the ablation plume has evolved for a further  $\sim 2 \mu\text{s}$  between the resonance ionization of Sr and Rb, and preferential ablation. Isotopic fractionation could, in principle, arise from the relative shifts in electronic transition energy from one isotope to another, owing to their different nuclear masses and volumes. However, our

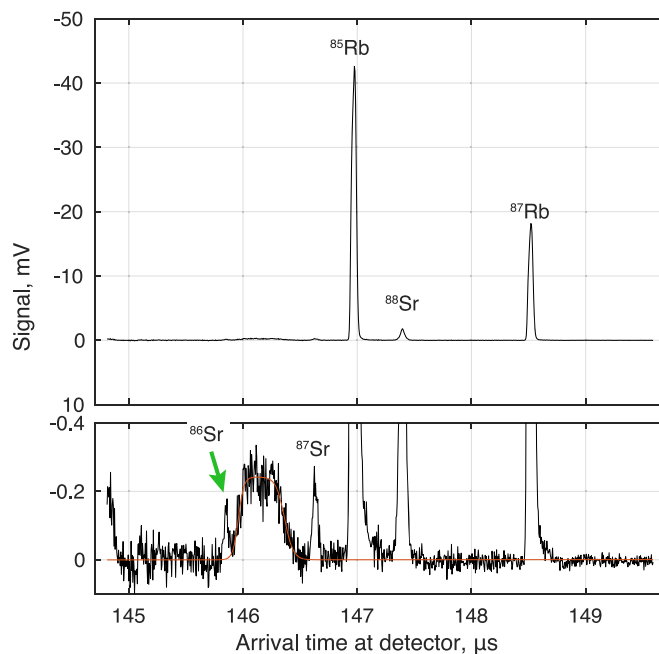


**Figure 4.** Time-of-flight spectrum for Pikes Peak Granite spot analysis 20190730ppg\_gsd-2g\_ras\_013, after subtracting measured backgrounds. The three most prominent peaks represent arrivals of resonance photoions of, from early to late,  $^{85}\text{Rb}$ ,  $^{88}\text{Sr}$ , and  $^{87}\text{Rb}$ . Top: spectrum at full scale. Bottom: baseline region of the same spectrum, showing the smaller peaks for  $^{86}\text{Sr}$  (green arrow) and  $^{87}\text{Sr}$  (146.6  $\mu\text{s}$ ) resonance photoions. The  $^{86}\text{Sr}$  peak sits on the shoulder of a broad peak which we ascribe to  $^{87}\text{Rb}$  ions created directly by ablation (the spectrum begins with the tail of the corresponding peak for  $^{85}\text{Rb}$ ). The red curve represents the empirical fit to the diffuse background for the interval in which the resonance photoions were arriving at the detector.

resonance lasers have linewidths of  $\sim 6 \text{ GHz}$ , much wider than the isotope shifts, and sufficient intensity to power-broaden their respective transitions. Instead, fractionation between the odd and even isotopes of Sr more likely arises from the different multiplicities of hyperfine states that can be populated during the resonance excitation process (e.g., Fairbank et al. 1989; Wunderlich et al. 1992). We corrected analyses of the granite samples to account for the measured instrumental sensitivities to each isotopic species.

## 4. Dating Granites with the CODEX Breadboard

### 4.1. Boulder Creek Granite

Our specimen of Boulder Creek Granite consists of potassium feldspar, quartz, plagioclase, and biotite, with grain sizes 2–10 mm (see Figure 2). In an earlier analytical campaign (Foster et al. 2016), we found an apparent age for Boulder Creek Granite of 3170 Ma, far in excess of the  $1700 \pm 40 \text{ Ma}$  age determined by Peterman et al. (1968). At issue, apparently, was the behavior of biotite under ablation by the laser we used at that time, which emitted 5 ns,  $\sim 250 \mu\text{J}$  pulses of 213 nm radiation. Biotite has a strong absorption band in this part of the ultraviolet spectrum (Karickhoff & Bailey 1973), and, indeed, biotite spot analyses yielded the largest signals for both Rb and Sr. Moreover, whereas spot analyses on other minerals demonstrated  $^{87}\text{Rb}/^{86}\text{Sr}$  ratios up to 1.5, biotite analyses yielded ratios as high as 30 (Figure 5). Therefore, the biotites dominated the best-line fit from which the age was calculated. However, their high  $^{87}\text{Rb}/^{86}\text{Sr}$  ratios were evidently not high enough to accord with the age found by Peterman et al. (1968).

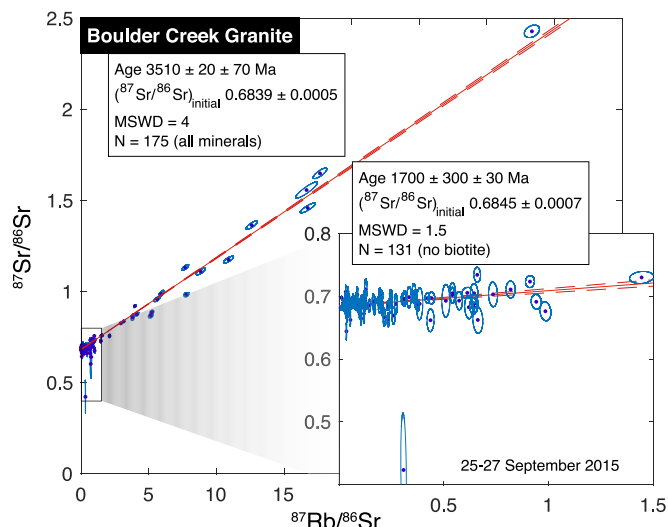


**Figure 5.** Our 2015 analysis of Boulder Creek Granite yielded an apparent age of 3510 Ma, but the isochron fit was controlled by analyses with very high  $^{87}\text{Rb}/^{86}\text{Sr}$  ratios, which were all identified as biotite on the basis of their laser-ablation mass spectra (Foster et al. 2016). Excluding those 44 analyses produces an isochron with an 1700 Ma age (inset). Note that an implausibly low intercept value is due to an unresolved  $\sim 3\%$  calibration issue among  $^{87}\text{Sr}/^{86}\text{Sr}$  ratios in this data set. Here and in subsequent figures, ages are quoted with their statistical uncertainties followed by systematic uncertainties, each representing  $1\sigma$  confidence intervals.

We understand this error in light of the differential ablation of Rb, which is more volatile, relative to Sr, which is more refractory, by nanosecond laser pulses. Whereas all mineral phases, and the glass standard we used, release Rb even at moderate ablation laser intensity, they release Sr more grudgingly. So long as it is common to all mineral phases, the preferential release of Rb is, in principle, accounted for by measuring instrumental fractionation of the elements with the glass standard. However, since biotite absorbed the ablation laser pulses more efficiently than the other phases, or than the glass standard, it was ablated at a higher effective temperature, where the preference for Rb over Sr was reduced. In this way, the standard-corrected  $^{87}\text{Rb}/^{86}\text{Sr}$  ratios we found for biotite were also reduced. Foster et al. (2016) showed that we could identify biotite spot analyses either on the basis of laser-ablation mass spectrometry, or by mapping the analyzed spots onto a photomicrograph of the specimen. Upon removing these biotite spot analyses from the isochron, we obtained an age of  $1700 \pm 300$  Ma (Figure 5, inset), which agrees with the age of Boulder Creek Granite found by Peterman et al. (1968).

Hydrated minerals such as biotite are conspicuously absent on the Moon (e.g., Papike et al. 1991). Therefore, the anomalous ablative behavior of this particular mineral will not compromise our ability to study lunar granites. Nevertheless, motivated by the observation that the ablative behavior of individual phases can vary so greatly, in 2019 we began a series of experiments with an ablation laser emitting 150 fs pulses in place of our nanosecond ablation laser. Whereas nanosecond laser ablation proceeds by the rapid thermalization of the deposited energy in a sample (Maul et al. 2005), leading atoms to “boil off,” femtosecond laser ablation delivers laser energy in less time than the typical interval between successive electron-lattice collisions (e.g., Gamaly et al. 2002a, 2002b). Because the energy is not thermalized, femtosecond ablation suddenly removes a large number of electrons from the sample surface, leading to a coulombic explosion (Husinsky et al.

2009), which is thought to release atoms more closely to their stoichiometric proportions. Indeed, many authors have found that elements are less fractionated one from another by femtosecond ablation than by nanosecond ablation (Riedo et al. 2013; Russo et al. 2013; Neuland et al. 2014).

Femtosecond laser ablation has two drawbacks for our purposes. First, as we have already noted, there are no spaceflight femtosecond laser systems suitable for CODEX presently available. Moreover, the femtosecond ablation process ionizes a greater fraction of the ablated atoms than does nanosecond ablation, which for resonance-ionization mass spectrometry is a source of noise. The present measurements were the first that we made with femtosecond ablation, and the spectra we obtained were noisy. In spite of this noise, we have for the first time been able to identify an isochron age for Boulder Creek Granite without having to remove all of the biotite analyses by hand (see Foster et al. 2016). We note in passing that we have subsequently learned to acquire cleaner spectra (e.g., Anderson et al. 2020b).

Data were acquired from Boulder Creek Granite in two runs, each employing slightly different tunings of the time-of-flight mass analyzer, as we iteratively tried to optimize the signal and suppress the noise from ions produced directly by ablation. In the first run, 2019 July 22–24, after subtracting the measured backgrounds, we found a diffuse residual swell in the background, which rose and fell on a timescale of several microseconds (e.g., Figure 3). In the example of Figure 3, background is responsible for  $\sim 0.02$  mV on peaks as small as  $\sim 0.6$  mV in amplitude; empirically removing this background therefore makes a difference of a few percent to some of the observed peak areas.

In between the two runs, the sample stub containing Boulder Creek Granite and GSD-2G was removed from the instrument, ground down by  $\sim 100 \mu\text{m}$  to remove the  $\sim 500$  ablation pits that had already been made, and reintroduced into the breadboard CODEX. In the second run, 2019 July 25–27, the mass spectrometer tunings were such that the diffuse background was more spread out in time, and over the  $5 \mu\text{s}$  interval of Sr and Rb photoion arrivals at the detector, the diffuse background was satisfactorily modeled as a straight line.

Our new analyses of the Boulder Creek Granite are shown in Figure 6, and are archived at Zenodo (doi:10.5281/zenodo.7742472). Of 800 spot analyses over the two runs, 635 detected the isotopes  $^{85,87}\text{Rb}$  and  $^{86,87,88}\text{Sr}$  at  $>2\sigma$  confidence, and of these, nine were discarded for having diffuse background noise that we could not well fit. All the remaining 626 spot analyses are represented in the figure. The best-fit line through the data implies an age of  $1780 \pm 110$  (statistical)  $\pm 300$  (systematic) Ma. We stress that the systematic uncertainty is due only to uncertainty in the composition of the GSD-2G standard; comparing with a better-known standard would eliminate this source of error. Our age agrees with the  $1700 \pm 40$  Ma age of Peterman et al. (1968). Moreover, the isochron line implies an initial  $^{87}\text{Sr}/^{86}\text{Sr}$  ratio of  $0.702 \pm 0.002$ , which likewise coincides with the value of 0.7035 inferred by Peterman et al. (1968).

Per usual, the linear fit, and thus the age, are heavily influenced by the most precisely measured points with especially high  $^{87}\text{Rb}/^{86}\text{Sr}$  ratios. Figure 6 demonstrates this by coloring the ellipse representing each measurement according to the amount by which the deduced rock age would have changed had that spot not been analyzed. This data set of 626

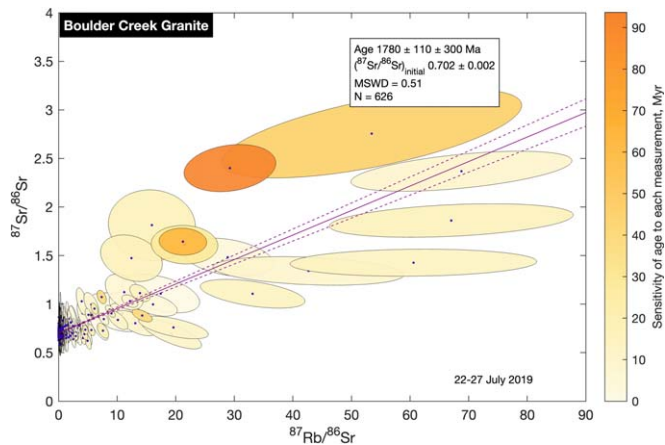


**Figure 6.**  $^{87}\text{Rb}$ - $^{87}\text{Sr}$  isochron for Boulder Creek Granite. Ellipses show  $1\sigma$  uncertainties for 626 individual spot analyses. The statistical uncertainty of 110 Myr arises from uncertainties in our measurements; the additional 300 Myr systematic uncertainty is due to the uncertainty in the concentrations of Rb and Sr in the standard GSD-2G. Analyses are colored by how sensitive the age of 1780 Ma is to the presence of each measurement in the ensemble of 626 (e.g., had we not sampled the spot with  $^{87}\text{Rb}/^{86}\text{Sr}$  ratio of 30 and  $^{87}\text{Sr}/^{86}\text{Sr}$  ratio of 2.5, we would have inferred an age 90 Myr younger).

spot analyses is relatively robust, because no single measurement affects the rock age by more than its statistical uncertainty of 110 Ma.

The spot analyses with the greatest uncertainties are those with the greatest  $^{87}\text{Rb}/^{86}\text{Sr}$  ratios, especially the five spots with  $^{87}\text{Rb}/^{86}\text{Sr} > 40$ . A high  $^{87}\text{Rb}/^{86}\text{Sr}$  ratio could be due, in principle, to either abundant Rb or scarce Sr, but in this case, all of these spots with high  $^{87}\text{Rb}/^{86}\text{Sr}$  ratios have particularly tiny Sr signals, just above the detection limit. Though their size on the isochron diagram makes them look important, if one were to ignore all five of these spots, the age implied by the best-fit line would change only slightly, to  $1680 \pm 110$  (statistical)  $\pm 300$  (systematic) Ma.

#### 4.2. Pikes Peak Granite

The Pikes Peak batholith includes rocks of two compositional suites, a potassic series and a sodic series. Our sample of Pikes Peak Granite is a hornblende granite whose feldspar crystals were 5–10 mm across (Figure 7). It was collected near the summit of Pikes Peak, close to where Hedge (1970) collected their sample 1221, an example of the potassic series. Hedge (1970) determined a whole-rock Rb–Sr isochron age of  $1041 \pm 13$  Ma for the batholith. Subsequent zircon analyses from the potassic series demonstrate an age of  $1066 \pm 10$  Ma, while other locations, including the sodic series, range from  $\sim 1060$ – $1090$  Ma (Guitreau et al. 2016 and references therein). Our typical precision does not distinguish among these ages.

As with the Boulder Creek Granite, data were acquired from Pikes Peak Granite in two runs with different tunings of the time-of-flight mass analyzer. Empirically we found that the diffuse background in the run of 2019 July 30 had the shape of a swell superimposed on a sloped line. We terminated this first run after 75 spot analyses on Pikes Peak Granite, in hopes that we could retune the mass analyzer for greater signal, and took advantage of the retuning hiatus to repolish the sample to a flat surface  $\sim 100 \mu\text{m}$  deeper. In the second run, 2019 August 6–8, the diffuse background was so slowly varying that we were able to model it as a straight line over the  $5 \mu\text{s}$  interval during which Sr and Rb photoions arrived at the detector.



**Figure 7.** Photomicrograph of standard GSD-2G (left) and Pikes Peak Granite (right). Note that the ablation pits in GSD-2G are hard to identify, and can just be made out on the granite (square box; compare with Figure 2). The ablation pits define a rectangular grid of points separated by 0.2 mm. The field of view is about 13 mm across.

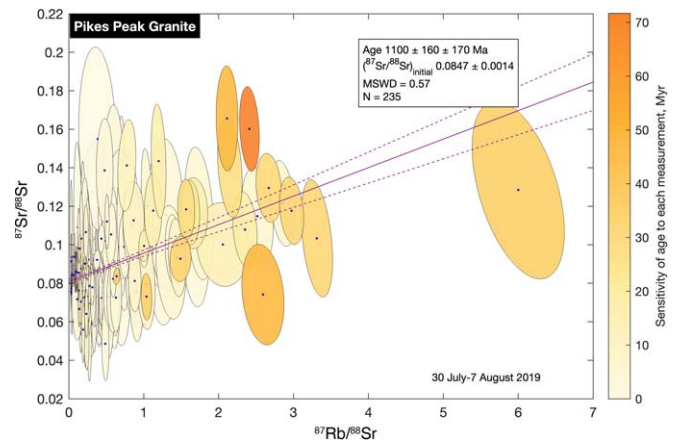


**Figure 8.**  $^{87}\text{Rb}$ - $^{87}\text{Sr}$  isochron for Pikes Peak Granite, showing 235 spot analyses and their  $1\sigma$  uncertainties. The uncertainty due to measurement imprecision is 160 Myr; another 170 Myr uncertainty is due to the uncertainty in the concentrations of Rb and Sr in the standard GSD-2G. Analyses are colored by how sensitive the age of 1100 Ma is to the presence of each measurement in the ensemble of 235 (e.g., had we not sampled the spot with  $^{87}\text{Rb}/^{86}\text{Sr}$  ratio of 6, we would have inferred an age 35 Myr older). Note that the illustrated isotope ratios are normalized to  $^{88}\text{Sr}$  as described in the text, rather than the customary  $^{86}\text{Sr}$ . Given the natural  $^{86}\text{Sr}/^{88}\text{Sr}$  ratio of 0.1194 (Meija et al. 2016), the initial  $^{87}\text{Sr}/^{88}\text{Sr}$  ratio of  $0.0847 \pm 0.0014$  inferred here implies an initial  $^{87}\text{Sr}/^{86}\text{Sr}$  ratio of  $0.709 \pm 0.011$ .

In addition to the diffuse background, there was also a discrete peak in the background, which interfered with our detection of  $^{86}\text{Sr}$  in these runs. We attribute the background peak to  $^{87}\text{Rb}$  ionized directly by the ablation pulse, because the background peak appears in spectra taken even when the resonance lasers for Rb and Sr are off. Ions produced directly by ablation ought to have been accounted for by subtraction of our measured backgrounds; however, during these runs, the over-detection of Rb relative to Sr was so great that even the shot-to-shot fluctuations in the  $^{87}\text{Rb}$  background peak overwhelmed our ability to quantify the resonantly ionized  $^{86}\text{Sr}$ . For this reason, we used  $^{88}\text{Sr}$  rather than  $^{86}\text{Sr}$  as a measure of stable, nonradiogenic Sr in our analysis (see Anderson et al. 2015b). Without a reliable measurement of  $^{86}\text{Sr}$ , we forewent the small correction to  $^{87}\text{Sr}$  that we make for mass-dependent fractionation among Sr isotopes.

Figure 8 illustrates our measurements of Pikes Peak Granite, and the data are also archived at Zenodo (doi:10.5281/zenodo.7742472). Out of 475 spot analyses in the two runs, only 260 yielded  $>2\sigma$  detections of all five of the isotopes  $^{85,87}\text{Rb}$  and

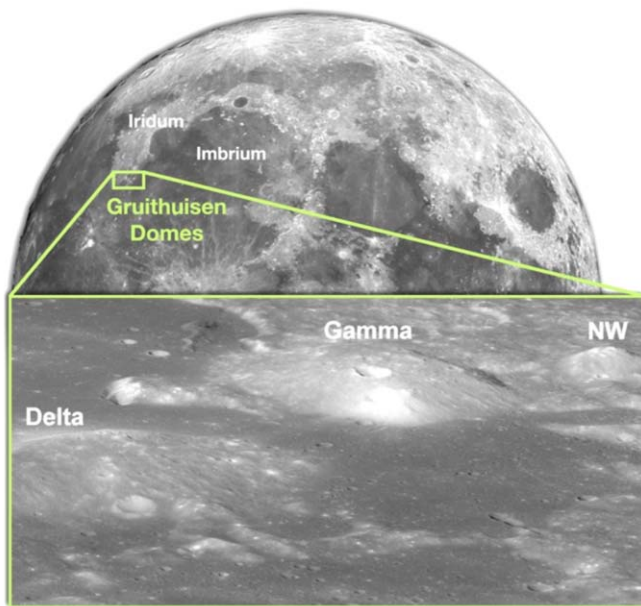


**Figure 9.** The Gruithuisen Domes: Delta, Gamma, and Northwest, as viewed by the Lunar Reconnaissance Orbiter Camera (Robinson et al. 2010).

$^{86,87,88}\text{Sr}$ . In 25 spot analyses, the diffuse background in a spectrum was poorly fit by our empirical function, so these spot analyses were discarded. The remaining 235 analyses are represented in Figure 8. The relatively low proportion of spot analyses in which the full set of isotopes was detected is, as noted above, likely due to the fact that a prism in the ablation beam path of the breadboard instrument was becoming coated by ablated atoms. The pattern of ablation pits in the Pikes Peak Granite (Figure 7) was much harder to see visually than in the Boulder Creek Granite (Figure 2), or than in our Zagami analyses (Anderson et al. 2015b), consistent with a reduction in ablation intensity from the prism becoming progressively sputter-coated with time.

The slope of the best-fit line through our data implies an age of  $1100 \pm 160$  (statistical)  $\pm 170$  (systematic) Ma. This agrees at the  $1\sigma$  level with the age of the Pikes Peak batholith as reported by Hedge (1970), Smith et al. (1999a, 1999b), and Guitreau et al. (2016). The intercept of  $0.0847 \pm 0.0014$  implies an initial  $^{87}\text{Sr}/^{86}\text{Sr}$  ratio of  $0.709 \pm 0.011$ , given the normal  $^{86}\text{Sr}/^{88}\text{Sr}$  ratio of 0.1194 (Meija et al. 2016). This coincides with the value of 0.7072 found by Hedge (1970). As for our Boulder Creek Granite isochron, this data set is robust, in that no single measurement affects the best-fit line by more than the quoted statistical uncertainty of 160 Myr.

## 5. A Mission to the Moon Using CODEX

### 5.1. Overview

We recently proposed CODEX as part of a lunar mission called ExCELL (Exploration of Chemically Evolved Lunar Lava), in order to determine the age and lithology of the Si-rich rocks that form the Gruithuisen Domes. The shapes of the Domes, and their composition inferred from orbital data (e.g., Figure 9), suggest that the rocks there are granitic, and yet granitic rocks are exceptionally rare (<0.02%) among Apollo samples (Seddio et al. 2013). Notable examples of these rare granites were first described by Ryder (1976), James & Hammarstrom (1977), Quick et al. (1982), and Warren et al.

(1983). Though Gruithuisen Domes appear, on the basis of crater density (Wagner et al. 2002; Braden 2013; Ivanov et al. 2016), to be younger than all dated Apollo granites (Seddio et al. 2013), did the Domes and the Apollo granites nevertheless evolve along similar petrogenetic pathways? Or will Gruithuisen Domes introduce us to a new lunar rock type, unknown from the Apollo collection? How and when were these extraordinary lunar volcanoes formed?

ExCELL would reveal the age and lithology of the Domes by landing on the surface of a dome and collecting and analyzing up to three 1.5–2.5 cm diameter rock samples to determine their radioisotopic ages, geochemistry, and normative mineralogy. Gamma Dome, which seems to have an exceptionally high concentration of thorium (Hagerty et al. 2006), is the most attractive landing site, because thorium concentration correlates in most lunar rocks with the abundance of rubidium, which is necessary for Rb–Sr dating.

ExCELL would accomplish its science goals using a payload comprising an arm-mounted rake guided by a ContextCam imager; a grinder; a second imager, MicroCam, for inspecting ground samples; and CODEX. For this mission, CODEX would alternate between resonance ionization of Rb and Sr isotopes for dating and laser-ablation mass spectrometry for chemical analysis and normative mineralogy. The geochemical data is valuable both for verifying inferences made by remote sensing from orbit, but also for contextualizing the geochronological data. For example, we showed above and in Foster et al. (2016) that identification of particular spot analyses as coming from a single mineral phase, in this case biotite, allowed us to extract meaningful dating information from the ensemble of remaining minerals.

In addition to the CODEX measurements, data from ContextCam would provide geological context for this unique lunar location. The rake and grinder would collect geotechnical data for the samples. MicroCam images taken before and after CODEX analysis would illustrate rock textures and mineral assemblages. The fusion of all of these results would allow us to ground-truth orbital observations, classify the rock type present at Gruithuisen Domes, compare with Apollo samples, identify when in lunar history these rocks formed, and test disparate crater-density age models.

The hardware for ExCELL includes a miniature (3.2 kg) time-of-flight mass analyzer built at the University of Bern (Wurz et al. 2012; Fausch et al. 2018), sample-handling systems made by Lockheed Martin Corporation, and custom spaceflight lasers designed by Aerospace Corporation. The spaceflight lasers are fiber master oscillator parametric amplifiers that have low mass (<20 kg) and low power consumption (<200 W), and boast higher stability and spectral intensity than the lasers in our breadboard version. Moreover, the spaceflight lasers will have a pulse rate of 1 kHz, allowing for more rapid data acquisition than our present 20 Hz instrument.

### 5.2. Mission Science

The composition inferred from orbital remote sensing makes Gruithuisen Domes unlike any of the sites visited by the Apollo missions, the samples from which have most strongly shaped our understanding of lunar evolution (Taylor 1975). Though the Apollo missions returned 382 kg of lunar samples, only 0.083 kg of these are granitic, and nearly all of the granitic material is from the single sample 12013 (e.g., Seddio et al.

2013). All of the granitic lunar samples were transported by impact ejection to the Apollo landing sites where they were collected, and most occur as clasts in polymict breccias (Seddio et al. 2013). Because of this, none of the Apollo granites have had their source rocks identified. Chemically, granitic lunar samples tend to have bulk composition with about 70 wt% SiO<sub>2</sub> and 60 ppm of Th (Seddio et al. 2013); the high Th concentration is comparable with what is inferred for the most enriched sites at Gruithuisen Domes (Hagerty et al. 2006).

There is no consensus on what processes generate chemically evolved, granitic magmas on the Moon. On Earth, partial melting in the interior can begin at relatively low temperature because water depresses the melting point of most rocks, generating magmas that readily incorporate silica and alkalis but that tend to leave magnesium- and calcium-rich minerals in the rock residua (Whitney 1988). However, this mechanism is not likely on the Moon because the bulk silicate Moon has only ~100 ppm of water (Barnes et al. 2016), compared with 2000 ppm in the bulk silicate Earth (Marty 2012). A more likely candidate is fractional crystallization of a basaltic magma, possibly with an admixture of KREEP material (e.g., Seddio et al. 2013), or the melting of lunar crust when underplated by basaltic intrusion (e.g., Hagerty et al. 2006; Gullikson et al. 2016). The evolution of magmas with SiO<sub>2</sub> as high as 70% may be aided by a miscibility gap between silicate liquids (Roedder 1951; Rutherford et al. 1974a, 1974b, 1976; Jolliff et al. 1999).

What little we presently know about the genesis of evolved lunar igneous rocks comes primarily from the few Apollo granites. Their radioisotopic ages suggest that they formed in two distinct epochs, an earlier one from 4400–4200 Ma, and a younger one from 4000–3850 Ma, with only a couple of examples in between (Meyer et al. 1996; Seddio et al. 2013, 2014; Zhang et al. 2012). This distribution of ages is similar to that of the giant impact basins on the Moon, but it has not yet been possible to test whether lunar granites were created by giant impacts. ExCELL, however, would probe a possible association between Gruithuisen Domes and the impact that formed Imbrium basin.

Because the Apollo granites are all fragments from unknown sources, we do not know the quantity of material produced by individual instances of granite formation on the Moon. However, if lunar granites formed by fractional crystallization, the parent basaltic magma must be at least an order of magnitude larger than the resulting granites. To build a granite body the size of Gruithuisen Domes in this way would therefore require an initial melt of ~10<sup>4</sup> km<sup>3</sup>. A large impact is a possible way to generate such a quantity of magma, either from direct heating or from decompression melting during excavation of the resulting crater (Grieve & Cintala 1992; Manske et al. 2022). Indeed, estimates of the volume of the Sudbury melt sheet, from one of the largest impacts known in Earth history, are of this scale (Latypov et al. 2019). Melting mechanisms internal to the Moon are also plausible, and large igneous provinces on Earth have erupted basalt volumes up to 10<sup>5</sup>–10<sup>6</sup> km<sup>3</sup>.

The location of Gruithuisen Domes presents two clues to their origin, but their implications seem mutually exclusive. First, Gruithuisen Domes are situated on the very margin of the Imbrium basin, the youngest of the giant impact basins on the nearside of the Moon. If the Imbrium melt sheet cooled slowly enough to undergo fractional crystallization, it perhaps could

have evolved a silica-rich composition like we infer for the Domes. For comparison, fractional crystallization has been invoked to explain the differentiation of the Sudbury melt sheet on Earth (Latypov et al. 2019). Since the cooling time of the Imbrium melt is likely ~1 Myr (Hood & Spudis 2016), this origin implies an age for the Domes that is indistinguishable from the 3920 Ma age inferred for Imbrium (Liu et al. 2012; Nemchin et al. 2021).

The second clue is that Gruithuisen Domes are surrounded by extensive flows of basaltic lava to which they may be petrogenetically related (e.g., Ivanov et al. 2016). For example, the granitic magma that formed the Domes may have been created by melting of crustal rocks when a basaltic magma welled up from deeper in the lunar interior and underplated the crust; if such underplating occurred, the basaltic magma could itself have erupted at the surface soon after the granitic magma (Lawrence et al. 2005; Hagerty et al. 2006; Ivanov et al. 2016). In this case, the Domes' age ought to be similar to the estimates for the basalt ages of 3600–2300 Ma, which are based on their crater densities (Ivanov et al. 2016).

CODEX has sufficient precision to resolve this age from the age of Imbrium (Figure 10). We have argued (Anderson et al. 2020b) that the measurement precision we achieved on Zagami would have yielded an age uncertainty of <80 Myr on a compositionally similar sample as old as 4500 Ma. In that work, we showed that femtosecond ablation was responsible for halving our age uncertainty, so we might expect ~160 Myr precision on a 3600–3900 Ma sample of Zagami-like composition using a spaceflight laser for nanosecond ablation. This is enough to distinguish, with 95% confidence, the age of Imbrium from the age of even the oldest of the surrounding basalts.

However, Gruithuisen Domes are likely to be much richer in Rb than is Zagami (~5.3 ppm; Barrat et al. 2001): if the usual scaling between Th and Rb concentrations (Haskin & Warren 1991; Neal 2022) holds, then the 35 ppm Th concentration inferred by Hagerty et al. (2006) implies a Rb concentration of 30–200 ppm at Gruithuisen Gamma. The much greater Rb abundance could easily improve our age uncertainty by a factor of 2 or more, permitting us to resolve ages in the middle of the 3920–3600 Ma interval from the age of either Imbrium or the surrounding basalts. Moreover, as contingency, we have sufficient time in the nominal mission plan to accommodate 1800 spot measurements on each sample, four times as many as in our Zagami experiment (Anderson et al. 2020b), potentially improving precision by another factor of 2. If we realize both of these factor-of-two improvements, we anticipate dating precision of ~40 Myr at Gruithuisen Domes.

If ExCELL finds that the age of Gruithuisen Domes implicates neither Imbrium nor the basalts in their formation, we would be forced to one of several more speculative explanations. Such an age could imply that the onset of basaltic volcanism in the region occurred earlier than 3600 Ma, but that the first basalts were buried beneath subsequent eruptions. Or, the basaltic magma might have underplated the crust and produced a granitic melt of crustal material, then remained molten but buried for a very considerable time before itself reaching the surface. This explanation is favored by some authors (e.g., Hagerty et al. 2006; Ivanov et al. 2016), but might become implausible if the measured age of the Domes requires an interval of more than a few tens of millions of years

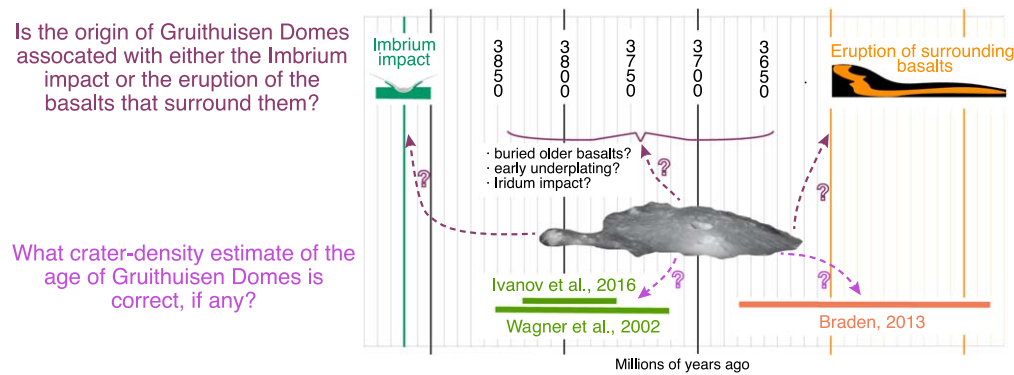


**Figure 10.** An ExCELL measurement of the age of Gruithuisen Domes would test the Domes' association with both the Imbrium impact and the eruption of nearby basalts, and also test competing estimates of their age based on densities of impact craters.

between the eruption of the Domes and the basalts. A third possibility is for the Domes to have been formed by the impact that excavated Sinus Iridum, somewhat later than Imbrium, likely in the interval 3840–3700 Ma (Wagner et al. 2002). However, this possibility is presently disfavored because Iridum was a considerably smaller impact than Imbrium, and the Domes are more than 200 km away from its rim rather than right on it, as for Imbrium.

Beyond testing associations between the Domes and Imbrium on the one hand, or the surrounding basalts on the other, radioisotopically dating Gruithuisen Domes would also test competing crater-density estimates of their age (Figure 10). For Gruithuisen Gamma, Wagner et al. (2002) used the density of craters to estimate an age of 3720–3850 Ma, and likewise Ivanov et al. (2016) deduced its age to be 3760–3830 Ma. However, Braden (2013) determined a considerably younger age of 3480–3670 Ma. Some of the uncertainty in each age estimate arises from the small number of craters on Gruithuisen Domes, but more stems from the different image sources that were used to count craters (e.g., Lunar Orbiter, Kaguya, or Lunar Reconnaissance Orbiter), different chronological models by which crater densities are associated with ages, and differences in how human observers recognize surface features as craters. While crater-density dating is generally believed to be more precise for the early Imbrian period than at other epochs, because models are calibrated on Apollo samples dated to this era (e.g., Stöffler et al. 2006), these estimates of the age of Gruithuisen Gamma nevertheless span 350 Myr. This is an indication of the magnitude of systematic uncertainties in crater-density dating. An ExCELL age for the Domes, by having been measured radioisotopically, would not be subject to these systematic uncertainties; rather, it would test which combinations of images, chronologies, and methodologies are accurate estimators of surface ages.

By using CODEX as a laser-ablation mass spectrometer, ExCELL would also measure elemental abundances in the rocks we sample, at the same spots analyzed for dating. At the whole-rock level, elemental abundances would determine the lithology of the samples and, coupled with rock textures imaged by the cameras, provide the most important clues for how the rocks formed. Our objectives are to characterize the lithology of each rock collected at the Domes, compositionally compare the samples to rock types represented in the Apollo collection, and to ground-truth the remote-sensing observations of exotic and silica-rich rocks at the Domes. A mundane but vital first objective is to ascertain that the sample collected by ExCELL actually represents the local rocks, rather than rocks

redistributed by impact ejecta. Given the spectral and morphological indications that Gruithuisen Domes is compositionally exceptional relative to all common lunar rock types, if we land on the Domes and collect a sample that is itself compositionally exceptional, we would have high confidence that it derives from the local bedrock. ExCELL measurements of silicon, iron and magnesium, calcium, aluminum, and alkali abundances would demonstrate whether the samples are chemically evolved, and therefore likely to derived from the Domes.

Likewise, measurements of major elements would situate the composition of the rocks on the total alkali-silica diagram. Precision achieved by ExCELL team members with a similarly miniaturized time-of-flight mass analyzer (Neuland et al. 2021) suggests we can measure  $\text{SiO}_2$  abundance with fractional uncertainty  $<5\%$ , and  $\text{Na}_2\text{O}$  and  $\text{K}_2\text{O}$  abundances with fractional uncertainties  $<10\%$ . This is sufficient to identify the composition as either basaltic, andesitic, dacitic, or granitic, for example (we do not expect to find more alkalic rock types). Images of the rock samples taken by MicroCam, with resolution of  $15 \mu\text{m}$  per pixel, would quantify the grain sizes of the mineral constituents in the rock, and therefore permit us to distinguish between fine-grained, extrusive rocks like basalt, andesite, and rhyolite, on the one hand, and their coarse-grained, intrusive analogs gabbro, diorite, and granite on the other.

Lithologic identification is important because different rock types require different formation processes. True rhyolites, for example, would seem to require fractional crystallization of a basaltic magma to run in excess of 90% (Hagerty et al. 2006). If the Domes are instead alkalic anorthosites, as suggested by Kaguya infrared observations that they are  $>80\%$  plagioclase (Lemelin et al. 2019), then they are more likely to be flotation cumulates (Shervais & McGee 1998). Moreover, to the extent that rocks from Gruithuisen Domes are lithologically similar to the Apollo granites, what we learn about their origin may help us understand the Apollo granites as well. If, conversely, the rocks sampled at Gruithuisen Domes are unlike any Apollo samples, the compositional data from ExCELL would characterize a new-to-science lunar rock type, broadening the range of geologic processes known to have been at work over the course of lunar history.

ExCELL measurements of major-element abundances in rocks from Gruithuisen Domes would also test inferences from remote sensing, such as the FeO abundance of 7%–9% deduced by Clementine (Lucy et al. 2000), Lunar Prospector (Hagerty et al. 2006), and Kaguya (Lemelin et al. 2019), and the  $\text{TiO}_2$

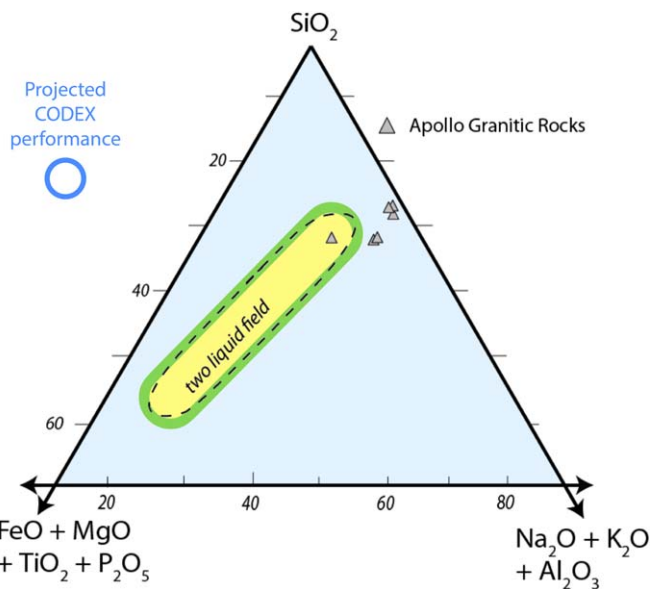


**Figure 11.** ExCELL would assess the evolution of the Domes composition by plotting oxide abundances on this ternary phase diagram (e.g., McCubbin et al. 2015). If the Domes' composition lies along the green boundary, then the granitic magma could have evolved by silicate liquid immiscibility. The size of the blue circle represents the anticipated precision of the CODEX measurement.

abundance of 0.7% derived from Chandrayaan-1 data (Kusuma et al. 2012). CODEX would be able to detect some important trace elements as well. For example, though Gruithuisen Domes are smaller than the footprint of the Lunar Prospector Gamma Ray Spectrometer, Hagerty et al. (2006) modeled a 35 ppm Th concentration for Gruithuisen Gamma; ExCELL data would evaluate this prediction. In addition, though ExCELL would measure elemental rather than mineralogical composition, ExCELL data could nevertheless test mineralogical inferences made by remote sensing. For example, if the Kaguya inference is correct that the surface rocks of Gruithuisen Gamma are ~80% plagioclase, then the oxide molar abundances of  $\text{Na}_2\text{O}$  and  $\text{CaO}$  must total ~16% (this value depends slightly on the mean molar mass of the rock); ExCELL would evaluate this. Significantly, CODEX ablates a few micrometers of material before beginning each spot analysis, so ExCELL data would pertain to the compositions of rocks; by contrast, visible and infrared observations from orbit are sensitive to the ubiquitous cover of lunar soil, which is depleted in volatile elements with respect to its parent rocks (Laul & Papike 1980).

Depending on the composition, the elemental abundances measured by ExCELL may yield clues about the petrogenesis of the samples, and by extension, of the Domes themselves. For example, there is considerable discussion in the literature about the role that silicate liquid immiscibility may have played in the evolution of granitic lunar magmas (Rutherford et al. 1976; Hagerty et al. 2006; Charlier & Grove 2012; Seddio et al. 2013; Gullikson et al. 2016). Finding a bulk-rock composition that lies near the boundary of the two-liquid miscibility gap (Figure 11) would favor this process in the evolution of the Domes (e.g., McCubbin et al. 2015), and finding a composition within the gap would rule it out.

Beyond measurements of age and composition, ExCELL would also deliver additional data about the rocks it samples and their geologic context. For example, MicroCam would

show the porosity of the rocks under analysis. ContextCam would help us learn geotechnical properties of the locality by observing the progress of the sampling rake as a function of applied current to its actuators as it penetrates the regolith, and the angle of repose of the regolith grains as the rake is emptied into the sample hopper. Moreover, ContextCam images would help the science team optimize science yield during mission operations by demonstrating relationships between the rocks collected for sampling at surface features such as impact craters, flank ridges, and boulders.

### 5.3. Mission Implementation

The ExCELL payload (Figure 12) would be delivered by a lunar lander to Gruithuisen Domes at local dawn and accomplish its entire mission in a single lunar day. Following the commissioning of the instruments, we would use ContextCam (Table 1) to observe the geologic context of the landing site and search for our first raking and acquisition area. A total of three samples would be raked, gripped, and ground by the Lockheed Martin-designed Preparation, Examination, Polishing and Retrieval (PEPR) system, imaged by MicroCam, and presented to CODEX for laser-ablation mass spectrometry and resonance-ionization mass spectrometry (Table 2).

The flight version of CODEX comprises laser and mass spectrometer subsystems. The laser subsystem, including its electronics, has been developed to TRL 5 by Southwest Research Institute and Aerospace Corporation (Di Teodoro et al. 2013; Mu et al. 2016a, 2016b, 2018), and brassboard prototypes of the lasers have passed three-axis vibrational testing at 6.8  $g_{\text{rms}}$  over the frequency range 5–3000 Hz. The lasers themselves are 1 kHz high-energy Yb-doped fiber master oscillator power amplifiers with spaceflight heritage. Six of the seven brassboard lasers have been shown to meet the functional requirements derived from our experience with the breadboard system for timing stability (<500 ns), bandwidth (8 GHz), frequency stability (drift <100 MHz per hour), beam quality ( $M^2 = 1.2$ ), and pulse energy (70–1000  $\mu\text{J}$ ). The 554 nm laser is still under development. The laser subsystem is to be hermetically sealed at 1 atm during the ExCELL mission to mitigate outgassing from laser components, and the flight design calls for it to be mounted directly on the lander deck for heat-sinking. Sealed windows permit laser light to pass directly into the mass spectrometer, mounted directly above the laser subsystem. The mass spectrometer has heritage from the ROSINA instrument on the ROSETTA mission (TRL 9; Scherer et al. 2006; Balsiger et al. 2007) and the Neutral Gas Mass Spectrometer (NGMS) on the Luna 25 and Luna 27 missions (Wurz et al. 2012). In 2016, the electrical engineering development unit from NGMS was mated to an ion source designed to accommodate both laser-ablation and resonance-ionization mass spectrometry, and these were successfully tested together on the CODEX breadboard.

The baseline mission requires the analysis of three unbrecciated centimeter-sized rocks with a science floor of a single sample. Based on the number density and size-distribution of rocks at the Surveyor landing sites, and the fraction of Apollo rocks that are unbrecciated, Anderson et al. (2017) estimated that raking the top 2 cm of lunar soil would yield about 60 unbrecciated centimeter-sized rocks per square meter. An alternative estimate of rock abundance, from Apollo cores, suggest that more than 300 rocks per square meter could be found in the near-surface (Cohen et al. 2021).

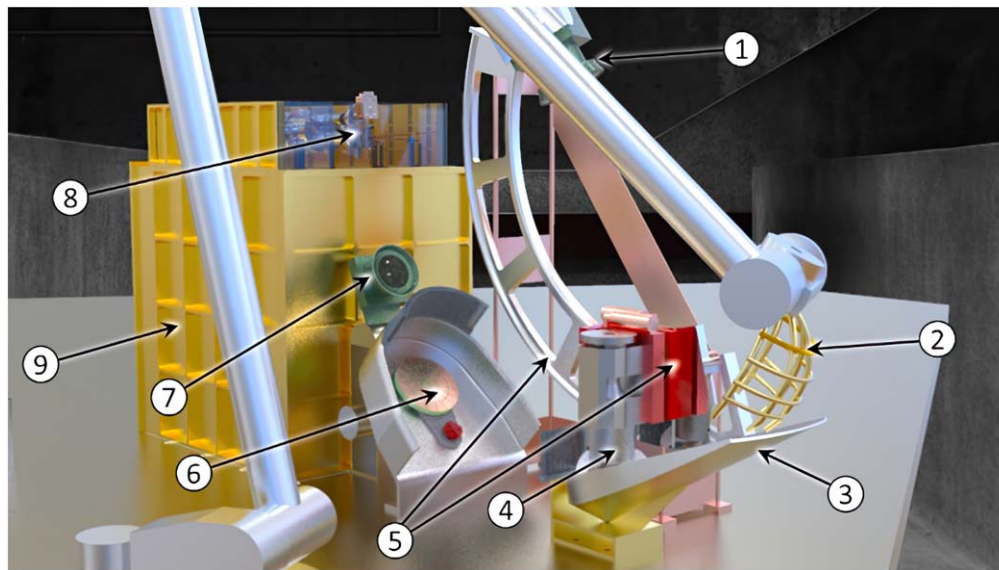


**Figure 12.** Computer rendering of the ExCELL instrument and manipulator arm. (1) Arm-mounted survey and selection ContextCam, (2) Sample rake, (3) Hopper, (4) Sample gripper, (5) X-Y stage and translation rail, (6) grinding station, (7) MicroCam sample inspection camera, (8) CODEX entrance aperture, and (9) laser housing. Front face of CODEX housing is transparent.

**Table 1**  
Instrument Suite and Function

| Instrument Suite and Function  |
|--|
| <b>1. ContextCam RGB Imager</b>  |
| • Autonomously construct mosaic image of landing site  |
| • Autonomously image surfaces around lander for raking area  |
| • Provide brief real-time video to assist raking, sample deposition in a hopper, gripping, and grinding                  |
| • Autonomous image of rake zone for geotechnical properties  |
| <b>2. Preparation, Examination, Polishing and Retrieval (PEPR) System</b>  |
| • Rake the surface with CLPS arm   |
| • Receive raked samples in hopper  |
| • Hold samples with gripper for MicroCam, Grinder, and CODEX   |
| • Grind flat face into samples for CODEX analysis  |
| • Carry mounted standard material for normalization of CODEX data  |
| <b>3. MicroCam RGB Imager (all autonomous)</b>   |
| • Image sample pre-grind for context   |
| • Image sample post-grind for grain size, rock type, and texture   |
| • Image sample post-CODEX for ablation spot location   |
| <b>4. CODEX</b>  |
| • Autonomously determine elemental abundances at up to 1800 spots by laser-ablation mass spectrometry                    |
| • Autonomously determine Rb-Sr isotope abundances at same spots by laser-ablation resonance-ionization mass spectrometry |

Guided by real-time images from ContextCam, we would rake appropriately sized rocks from the upper 2 cm of the surface, and bring them to the PEPR system hopper (Figure 12). The PEPR system would grasp a rock and transfer it to the grinding station to create a smooth face in the rock with  $<15 \mu\text{m}$  rms roughness, suitable for laser ablation. MicroCam would inspect the polished surface, and image the grain size and texture of the polished rock samples. ContextCam images would undergo lossy compression to permit rapid downlink at  $\sim 1$  frame per second, with losslessly compressed images buffered for later downlink. MicroCam images would be immediately downloaded at full resolution and reviewed prior to moving on from grinding operations.

After grinding, polishing, and imaging, the sample would be moved to the focal plane of the CODEX ablation laser. We would translate the gripper in that plane to obtain at least 400 spot analyses on a  $25 \text{ mm}^2$  region of the sample. After every four analyses of the rock, the gripper would translate further to analyze a standard mounted on the side of the gripper. Finally, the sample would be returned to MicroCam which would record the locations of the ablation spots relative to observed mineral grains, before the rock is ejected and the process is repeated with a new sample as time and data downlink permit. Images would be relayed to the ground during the sample selection, acquisition, post-grind inspection, and post ablation inspection. Other operations are autonomous.

Interpretation of the collected data from each sample would include inferences about whether a deduced age represents the timing of crystallization or a secondary shock event. To maximize the probability that ages measured by CODEX pertain to crystallization of the volcanic rocks at Gruithuisen Domes, ExCELL mission plans call for observations of each sample's geologic context, using ContextCam, and analysis of multiple rock samples, using CODEX and MicroCam. Priority during sample collection would be given to rocks that appear typical of the locality. Even before beginning a time-consuming CODEX analysis, we would inspect MicroCam images for evidence that a sample is brecciated; breccias are more likely to have been shocked. We would examine the Rb and Sr isotopic data acquired by CODEX to learn whether particular mineral phases depart from an isochron line; if spot analyses corresponding to one geochemical composition fall off the isochron defined by other phases, it could be evidence of alteration by shock. Likewise, we would compare CODEX-derived chemical compositions with inferences made from orbital remote sensing to help recognize whether a sample is locally derived. Finally, finding the same age for several samples would favor their age representing a common crystallization event, since the stochastic process of remobilization of  $^{87}\text{Sr}$  by a passing shock wave is unlikely to yield a reproducible age among an ensemble of samples. In summary,

**Table 2**  
Time and Data Requirements for ExCELL Activities on the Lunar Surface

|   | Activity Nominal Time<br>(hours:minutes) | Attempts with<br>Contingency | Time with Contingency (hours:<br>minutes) | Data (MB) |
|---|--|------------------------------|---|-----------|
| Commissioning   | 8:00                                     | 1                            | 8:00                                      | 1         |
| Image scene   | 0:05                                     | 1                            | 0:05                                      | 20        |
| Rake & drop samples onto tray, including real-time videolink  | 0:05                                     | 9                            | 0:45                                      | 200       |
| Image tray  | 0:01                                     | 9                            | 0:09                                      | 20        |
| Select rock from tray for analysis                            | 0:20                                     | 9                            | 3:00                                      | ...       |
| Grip and pick up selected rock, including real-time videolink | 0:05                                     | 9                            | 0:45                                      | 200       |
| Image gripped rock  | 0:01                                     | 9                            | 0:09                                      | 20        |
| Confirm rock is successfully gripped                          | 0:20                                     | 9                            | 3:00                                      | ...       |
| Grind rock sample   | 2:00                                     | 3                            | 6:00                                      | 5         |
| Image ground rock surface                                     | 0:01                                     | 3                            | 0:03                                      | 20        |
| CODEX analysis (up to 1800 spots)                             | 23:40                                    | 1                            | 23:40                                     | 4 625     |
| Image rock surface with analysis pits                         | 0:01                                     | 1                            | 0:01                                      | 20        |
| Drop sample   | 0:01                                     | 3                            | 0:03                                      | 2         |
| Total for first rock, including commissioning                 | 34:40                                    |                              | 44:40                                     | 5 133     |
| Total for second and third rocks, raked and imaged together   | 52:44                                    |                              | 67:32                                     | 10 004    |
| Total   | 87:24                                    |                              | 112:12                                    | 15 137    |
| Total available (9 Earth days)                                | 216:00                                   |                              | 216:00                                    | 21 870    |
| Margin  | 60%                                      |                              | 48%                                       | 31%       |

we would use the totality of the evidence to interpret whether a sample has yielded a shock age or a crystallization age; this is analogous to the ongoing interpretation of the geologic and petrologic context of the recently acquired samples from Chang'e 5. Both crystallization ages and shock ages are potentially significant for answering science questions.

If none of the contingency time built into our surface operations plan were necessary, we would have sufficient time in nine Earth days to analyze 10 rock samples. Known contingencies include multiple attempts for raking, picking up, and grinding rocks; allowing time for nine raking and pickup attempts, and three grindings attempts (Table 2), we would still have sufficient time to study three rocks (4.7 Earth days) with margin for unknown contingencies of 4.3 Earth days (48%). Data downlink puts a stronger limit on what ExCELL can accomplish, however. Assuming an average downlink rate of  $225 \text{ kbit s}^{-1}$ , the entire data volume that can be returned in 9 Earth days is 22 GB. Analysis of three samples would include just over 15 GB of data, leaving a 30% margin.

## 6. Conclusion

The dating precision attainable with CODEX has advanced to the point where statistical errors are now comparable to those arising from uncertainties in the composition of reference materials used for calibration. This highlights a need for better characterization of standard materials with geologically realistic concentrations of Rb and Sr, and we hope that the

geostandards community will continue to make progress toward this aim.

The development of CODEX for spaceflight continues on two fronts. First, we continue to demonstrate the ability of CODEX to analyze ever-more-challenging planetary-analog samples with the breadboard instrument. Our successful dating of two granite samples is part of this effort. Though we had expected that granites would have been relatively easy to analyze because of their relatively high concentration of Rb, we were challenged by the fact that biotite behaved differently from other materials under nanosecond laser ablation, and then by noisy diffuse backgrounds of ions generated by femtosecond ablation. Though biotite delayed this demonstration of CODEX capabilities with terrestrial samples, it is, like other hydrated minerals, unknown on the Moon. As for the diffuse ion background, we have shown here that empirical fitting of it permitted us to date accurately both Boulder Creek Granite and Pikes Peak Granite, in spite of the elevated noise.

Second, the work of miniaturization continues. Whereas the breadboard instrument has a mass spectrometer of length 1 m and mass 40 kg, the flight instrument is designed with heritage parts from ROSETTA and other missions that are 0.2 m long and have only 3.2 kg of mass. Our breadboard uses seven lasers that are 35 kg each, but the brassboard MOPA lasers have a mass of about 20 kg *total*. By increasing our laser pulse rate from 20 Hz to 1 kHz, these lasers also increase the quantity of data that can be acquired, even if a mission is limited to a single

lunar day. The ExCELL mission to the Gruithuisen Domes would deliver geochemical and geochronological data, with field context, that would allow us to understand the origin of evolved igneous rocks on the Moon.

We thank the US NASA science and instrument development programs for supporting this work, including PIDD Program grants NNX10AJ87G, NNX08AT61G, NNX08AZ14G, PICASSO Program grants 80NSSC17K0585 and 80NSSCC17K0099, MatISSE Grants 80NSSC18K0131, NNX15AF41G, DALI grant 80NSSC21K0743, and SSW grant 80NSSC22K0108. We thank the Pikes Peak Lands and Minerals Staff Officer Jeffrey Hovermale for permission to collect a sample of the Pikes Peak Granite. Dr. Anderson is grateful to years of support and friendship from Dr. Whitaker, and congratulates him on his retirement. Dr. Levine thanks the Colgate University Faculty Research Council for a Picker fellowship. Dr. Joy is funded by a Royal Society University Research Fellowship (URF\R\201009), and both Dr. Joy and Dr. Pernet-Fisher are funded by Science and Technology Facilities Council grant ST/V000675/1. All of the authors express our collective appreciation of T. Erickson and an anonymous reviewer for thoughtful, helpful, and gracious reviews of the manuscript.

### ORCID iDs

Rico G. Fausch  <https://orcid.org/0000-0001-9638-806X>

Peter Wurz  <https://orcid.org/0000-0002-2603-1169>

### References

- Alvarez, L. W., Alvarez, W., Asaro, F., & Michel, H. V. 1980, *Sci*, **208**, 1095
- Anderson, F. S., Crow, C., Levine, J., & Whitaker, T. J. 2020a, *E&SS*, **7**, e2020EA001177
- Anderson, F. S., Levine, J., & Whitaker, T. 2020b, *P&SS*, **191**, 105007
- Anderson, F. S., Levine, J., & Whitaker, T. J. 2015a, *RCMS*, **29**, 191
- Anderson, F. S., Levine, J., & Whitaker, T. J. 2015b, *RCMS*, **29**, 1457
- Anderson, F. S., Whitaker, T., Miller, G., et al. 2003, *AGUFM*, **41**, P41B-0412
- Anderson, F. S., Whitaker, T. J., & Levine, J. 2017, *LPSC*, **48**, 2957
- Balsiger, H., Altwegg, K., Bochsler, P., et al. 2007, *SSRv*, **128**, 745
- Barnes, J. J., Kring, D. A., Tartèse, R., et al. 2016, *NatCo*, **7**, 11684
- Barrat, J. A., Blichert-Toft, J., Nesbitt, R. W., & Keller, F. 2001, *M&PS*, **36**, 23
- Bechtold, A., Brandstätter, F., Pittarello, L., et al. 2021, *M&PS*, **56**, 971
- Braden, S. E., & Robinson, M. S. 2011, *GSASP*, 483, 507
- Braden, S. E., Stopar, J. D., Robinson, M. S., et al. 2014, *NatGe*, **7**, 787
- Braden, S. E. 2013, PhD thesis, Arizona State Univ.
- Charlier, B., & Grove, T. L. 2012, *CoMP*, **164**, 27
- Che, X., Nemchin, A., Liu, D., et al. 2021, *Sci*, **374**, 887
- Cohen, B. A., Young, K. E., Zellner, N. E. B., et al. 2021, *PSJ*, **2**, 145
- Culler, T. S., Becker, T. A., Muller, R. A., & Renne, P. R. 2000, *Sci*, **287**, 1785
- Di Teodoro, F., Morais, J., McComb, T., et al. 2013, *OptL*, **38**, 2162
- Du, J., Fa, W., Gong, S., et al. 2022, *JGRE*, **127**, e2022JE007314
- Eberhardt, P., Geiss, J., Grögler, N., & Stettler, A. 1973, *Moon*, **8**, 104
- Fairbank, W., Spaar, M., Parks, J., & Hutchinson, J. 1989, *PhRvA*, **40**, 2195
- Fassett, C. I., Kadish, S. J., Head, J. W., Solomon, S. C., & Strom, R. G. 2011, *GeoRL*, **38**
- Faure, G. 1986, *Principles of Isotope Geology* (2nd ed.; New York: Wiley)
- Fausch, R., Wurz, P., Tulej, M., et al. 2018, *EGUGA*, **20**, 13231
- Foster, S., Levine, J., Anderson, F., & Whitaker, T. 2016, *LPSC*, **47**, 2070
- Gamaly, E. G., Rode, A. V., Luther-Davies, B., & Tikhonchuk, V. T. 2002a, *PhPl*, **9**, 949
- Gamaly, E. G., Rode, A. V., Tikhonchuk, V. T., & Luther-Davies, B. 2002b, *ApSS*, **197**, 699
- Glotch, T. D., Lucey, P. G., Bandfield, J. L., et al. 2010, *Sci*, **329**, 1510
- Grange, M. L., Nemchin, A. A., & Pidgeon, R. T. 2013, *JGRE*, **118**, 2180
- Greenhagen, B., Lucey, P., Wyatt, M., et al. 2010a, *AAS/DPS Meeting*, **42**, 979
- Greenhagen, B. T., Lucey, P. G., Wyatt, M. B., et al. 2010b, *Sci*, **329**, 1507
- Grieve, R. A. F., & Cintala, M. J. 1992, *Metic*, **27**, 526
- Grove, T. L., & Krawczynski, M. J. 2009, *Elem*, **5**, 29
- Guitreau, M., Mukasa, S. B., Blichert-Toft, J., & Fahnstock, M. F. 2016, *PreR*, **280**, 179
- Gullikson, A. L., Hagerty, J. J., Reid, M. R., Rapp, J. F., & Draper, D. S. 2016, *AmMin*, **101**, 2312
- Hagerty, J. J., Lawrence, D., Hawke, B., et al. 2006, *JGRE*, **111**
- Hartmann, W. K., Strom, R. G., Weidenschilling, S. J., et al. 1981, *Basaltic Volcanism on the Terrestrial Planets* (New York: Pergamon), 1049
- Haskin, L., & Warren, P. 1991, *Lunar Chemistry, Lunar Sourcebook*, Vol. 4 (Cambridge: Cambridge Univ. Press), 357
- Hedge, C. 1970, *USGSP*, 700, B86
- Hiesinger, H. V., Van Der Bogert, C., Pasckert, J., et al. 2012, *JGRE*, **117**
- Hood, L. L., & Spudis, P. 2016, *JGRE*, **121**, 2268
- Husinsky, W., Bashir, S., Rafique, M. S., & Ajami, A. 2009, in 4th Int. Conf. Laser Probing -LAP 2008, 1104, 79
- Ivanov, M., Head, J., & Bystrov, A. 2016, *Icar*, **273**, 262
- James, O. B. 1982, *LPSC*, **12**, 209
- James, O. B., & Hammarstrom, J. G. 1977, *LPSC*, **8**, 2459
- Jochum, K. P., Wilson, S. A., Abouchami, W., et al. 2011, *GGRes*, **35**, 193
- Jolliff, B., Floss, C., McCallum, I., & Schwartz, J. 1999, *AmMin*, **84**, 821
- Jolliff, B. L., Gillis, J. J., Haskin, L. A., Korotev, R. L., & Wiczorek, M. A. 2000, *JGR*, **105**, 4197
- Karickhoff, S. W., & Bailey, G. W. 1973, *CCM*, **21**, 59
- Kusuma, K., Sebastian, N., & Murty, S. 2012, *P&SS*, **67**, 46
- Laneville, M., Wiczorek, M. A., Breuer, D., & Tosi, N. 2013, *JGRE*, **118**, 1435
- Latypov, R., Chistyakova, S., Grieve, R., & Huhma, H. 2019, *NatCo*, **10**, 508
- Laul, J. C., & Papike, J. J. 1980, *LPSC*, **11**, 1307
- Lawrence, D., Elphic, R., Feldman, W., et al. 2003, *JGRE*, **108**
- Lawrence, D., Hawke, B., Hagerty, J., et al. 2005, *GeoRL*, **32**
- Lawrence, D., Puetter, R., Elphic, R., et al. 2007, *GeoRL*, **34**
- Lemelin, M., Lucey, P. G., Miljković, K., et al. 2019, *P&SS*, **165**, 230
- Levine, J., Becker, T. A., Muller, R. A., & Renne, P. R. 2005, *GeoRL*, **32**, 4
- Li, Q.-L., Zhou, Q., Liu, Y., et al. 2021, *Natur*, **600**, 54
- Liu, D., Jolliff, B. L., Zeigler, R. A., et al. 2012, *E&PSL*, **319**, 277
- Lucey, P. G., Blewett, D. T., & Jolliff, B. L. 2000, *JGRE*, **105**, 20297
- Manske, L., Wünnemann, K., & Kurosawa, K. 2022, *JGRE*, **127**, e2022JE007426
- Marty, B. 2012, *E&PSL*, **313**, 56
- Maul, J., Karpuk, S., & Huber, G. 2005, *PhRvB*, **71**, 045428
- Mazrouei, S., Ghent, R. R., Bottke, W. F., Parker, A. H., & Gernon, T. M. 2019, *Sci*, **363**, 253
- McCubbin, F. M., Vander Kaaden, K. E., Tartèse, R., et al. 2015, *AmMin*, **100**, 1668
- McEwen, A. S., Moore, J. M., & Shoemaker, E. M. 1997, *JGR*, **102**, 9231
- Meija, J., Coplen, T. B., Berglund, M., et al. 2016, *P&PCh*, **88**, 293
- Meyer, C., Williams, I. S., & Compston, W. 1996, *M&PS*, **31**, 370
- Mu, X., Crain, W., Nguyen, C., et al. 2018, *Proc. SPIE*, **10512**, 1051211
- Mu, X., Steinvurzel, P., Belden, P., et al. 2016a, in *OSA Laser Congress 2016* (Boston, MA: OSA) LW3B.2
- Mu, X., Steinvurzel, P., Rose, T. S., et al. 2016b, *Proc. SPIE*, **9731**, 973108
- Neal, C. 2022, *Mare Basalt Database (Major & Trace Elements)* [retrieved 2022 November 29], <https://www3.nd.edu/cneal/Lunar-L/Mare-Basalt-Database.xls>
- Nemchin, A. A., Long, T., Jolliff, B. L., et al. 2021, *ChEG*, **81**, 125683
- Neukum, G. 1977, *Moon*, **17**, 383
- Neukum, G., Ivanov, B. A., & Hartmann, W. K. 2001, *SSRv*, **96**, 55
- Neukum, G., König, B., & Arkan-Hamed, J. 1975, *Moon*, **12**, 201
- Neuland, M., Meyer, S., Mezger, K., et al. 2014, *P&SS*, **101**, 196
- Neuland, M., Mezger, K., Riedo, A., Tulej, M., & Wurz, P. 2021, *P&SS*, **204**, 105251
- Norman, M. D. 2009, *Elem*, **5**, 23
- Papike, J., Taylor, L., & Simon, S. 1991, *Lunar Sourcebook: A user's Guide to the Moon* (Cambridge: Cambridge Univ. Press), 121
- Peterman, Z. E., Hedge, C. E., & Braddock, W. A. 1968, *JGR*, **73**, 2277
- Quick, J., James, O., & Albee, A. 1982, *LPSC*, **12**, 117
- Riedo, A., Neuland, M., Meyer, S., Tulej, M., & Wurz, P. 2013, *Journal of Analytical Atomic Spectrometry*, **28**, 1256
- Robinson, M. S., Brylow, S. M., Tschimmel, M., et al. 2010, *SSRv*, **150**, 81
- Robbins, S. J. 2014, *E&PSL*, **403**, 188
- Roedder, E. 1951, *AmMin*, **36**, 282
- Russo, R. E., Mao, X., Gonzalez, J. J., & Yoo, J. 2013, *Spectroscopy*, **28**, 24, <https://www.spectroscopyonline.com/view/femtosecond-vs-nanosecond-laser-pulse-duration-laser-ablation-chemical-analysis>
- Rutherford, M., Hess, P., & Daniel, G. 1974a, *LPSC*, **5**, 657

- Rutherford, M. J., Hess, P. C., Ryerson, F. J., Campbell, H. W., & Dick, P. A. 1976, *LPSC*, **7**, 1723
- Rutherford, M., Hess, P. C., & Daniel, G. H. 1974b, *LPSC*, **5**, 569
- Ryder, G. 1976, *E&PSL*, **29**, 255
- Ryder, G., Stoesser, D. B., Marvin, U. B., & Bower, J. 1975, *LPSC*, **6**, 435
- Schaeffer, O., & Husain, L. 1974, *LPSC*, **5**, 1541
- Scherer, S., Altwegg, K., Balsiger, H., et al. 2006, *IJMSp*, **251**, 73
- Seddio, S. M., Jolliff, B. L., Korotev, R. L., & Carpenter, P. K. 2014, *GeCoA*, **135**, 307
- Seddio, S. M., Jolliff, B. L., Korotev, R. L., & Zeigler, R. A. 2013, *AmMin*, **98**, 1697
- Sephton, M. A., Waite, J. H., & Brockwell, T. G. 2018, *AsBio*, **18**, 843
- Shervais, J. W., & McGee, J. J. 1998, *GeCoA*, **62**, 3009
- Shoemaker, E. M., & Hackman, R. J. 1962, in *IAU Symp. 14, The Moon*
- Smith, D. R., Noblett, J., Wobus, R. A., Unruh, D., & Chamberlain, K. R. 1999a, *RMGeo*, **34**, 289
- Smith, D. R., Noblett, J., Wobus, R.A., et al. 1999b, *PreR*, **98**, 271
- Spudis, P. D., Wilhelms, D. E., & Robinson, M. S. 2011, *JGRE*, **116**
- Stöffler, D., Ryder, G., Ivanov, B. A., et al. 2006, *RvMG*, **60**, 519
- Tartèse, R., Anand, M., Gattacceca, J., et al. 2019, *SSRv*, **215**, 1
- Taylor, S. R. 1975, *Lunar Science: A Post-Apollo View; Scientific Results and Insights from the Lunar Samples* (New York: Pergamon)
- Tera, F., Papanastassiou, D., & Wasserburg, G. 1974, *E&PSL*, **22**, 1
- Thiessen, F., Nemchin, A. A., Snape, J. F., Bellucci, J. J., & Whitehouse, M. J. 2018, *GeCoA*, **230**, 94
- Tian, H.-C., Wang, H., Chen, Y., et al. 2021, *Natur*, **600**, 59
- Villa, I. M., De Bièvre, P., Holden, N. E., & Renne, P. R. 2015, *GeCoA*, **164**, 382
- Wagner, R., Head, J. W., III, Wolf, U., & Neukum, G. 2002, *JGRE*, **107**
- Warren, P. H., Taylor, G. J., Keil, K., Shirley, D. N., & Wasson, J. T. 1983, *E&PSL*, **64**, 175
- Whitney, J. A. 1988, *GSAB*, **100**, 1886
- Wieczorek, M. A., & Phillips, R. J. 2000, *JGRE*, **105**, 20417
- Wilhelms, D. E., McCauley, J. F., & Trask, N. J. 1987, *The Geologic History of the Moon* Professional Paper 1348USGS
- Wilson, S. 2018, G-probe 20 summary report (GSD-2G), [accessed 2022], International Association of Geoanalysts, <http://www.geoanalyst.org/wp-content/uploads/2021/02/GP-20-report.pdf>
- Wöhler, C., Lena, R., Lazzarotti, P., et al. 2006, *Icar*, **183**, 237
- Wunderlich, R. K., Wasserburg, G. J., Hutcheon, I. D., & Blake, G. A. 1992, in *Resonance Ionization Spectroscopy 1992 (Santa Fe, NM, 1992 May 24-29)* 127
- Wurz, P., Abplanalp, D., Tulej, M., & Lammer, H. 2012, *P&SS*, **74**, 264
- Yue, Z., Di, K., Wan, W., et al. 2022, *NatAs*, **6**, 541
- Zellner, N. E. 2017, *OLEB*, **47**, 261
- Zeng, X., Li, X., Xia, X. P., et al. 2021, *GeoRL*, **48**, e2021GL092639
- Zhang, A.-C., Taylor, L. A., Wang, R.-C., et al. 2012, *GeCoA*, **95**, 1